BIU-YU STUDENT RESEARCH SYMPOSIUM

AUGUST 10-11

A Collection of Research Abstracts from the BIU-YU Summer Science Research Internship 2014

Av & Em Bayit:
Rav Eliav and Adi

Program Director:
Prof. Ari Zivotofsky

Program Founder:
Prof. Chaim Sukenik

The BIU-YU Summer Science Research Internship Program places select undergraduates in state-of-the-art research laboratories of Bar-Ilan's Life Science, Exact Science, or Engineering Faculties. The program enables talented undergraduate science majors to take part in the research of one of Bar-Ilan's more than 180 distinguished science and engineering faculty members. The BIU-YU Summer Science Research Internship Program is partially funded by the Bar-Ilan Global Board of Trustees Chairman, Dr. Mordecai D. Katz, and his wife Dr. Monique Katz, and by the J. Samuel Harwit, zt"l & Manya Harwit Aviv Charitable Trust.

TABLE OF CONTENTS

CHEMISTRY / PHYSICS

COMPUTER SCIENCE / ENGINEERING

LIFE SCIENCES

NEUROSCIENCE / PSYCHOLOGY

Edited, compiled and designed by Talia Felman, Jennifer Grossman, Alexander Straus, and Michal Schechter. Photos: Yaron Milwid.

CHEMISTRY / PHYSICS

Left to right: T. Cohn, D. Kaplan, C. Metzger, Z. Moldwin, S. Kay, T. Felman

ELECTROCHEMISTRY :: AURBACH LAB

Jake Abitol (Yeshiva College) "Multidisciplinary Battery Development for a More Energy Efficient Future."

Professor Aurbach's research in electrochemistry is focused on inventing novel chemistries for Lithium-ion battery technology- the technology powering the mobile electronics and electric vehicle markets. Much more than finding the most efficient electrode/ electrolyte couplings, this work requires a combination of chemistry, physics, and engineering. In fact, one of the key areas being investigated currently is the nanostructure of the surface of electrodes. While redox couples and electrolyte chemistries are extremely important, the way in which ions are transferred depends largely on the structures of interfacial surfaces. Therefore, one major focus of Professor Aurbach's lab is analyzing different possible surface structures that can result from various preparation processes.

CHEMISTRY AND NANOTECHNOLOGY :: LELLOUCHE LAB

Thomas Cohn (Cornell University) "Functionalization of WS_2 Inorganic Nanotubes and WS_2 Inorganic Fullerene Nanoparticles with Maghemite (γ-Fe_2O_3)"

WS_2 Inorganic Nanotubes (INT) and WS_2 Inorganic Fullerene (IF) nanoparticles are currently being researched for their potential use as nanoscale fillers for polymeric matrices. If the INT and IF can be successfully functionalized by attaching desired functional groups to their surfaces, then they can be integrated into polymers to create new materials with desired novel sets of properties. The resultant composite materials with improved mechanical and tribiological properties would have a whole host of applications ranging from micro-electrical mechanical devices to macro-scale biomedical apparatuses.

Researchers are currently faced with the challenge of how to attach desired functional groups to the INT and IF surfaces due to the inability of said functional groups to bond directly to the INT and IF surfaces. The goal of this research was to solve this problem by connecting to the INT and IF a material that can serve as a bridge between the INT and IF surface and the desired functional groups. If chemical bonds between the surface of the INT or IF and various forms of maghemite (γ-Fe_2O_3) could be formed, then the resultant maghemite coating could serve as an interfacial platform upon which functional groups could be added. Two distinct methods were used to accomplish this goal. The first method involved mixing the WS_2 INT and WS_2 IF in aqueous solution with CAN-maghemite (γ - Fe_2O_3) nanoparticles (NP), maghemite NP whose surface had been doped with cerium 3/4 + cations. The pre-formed NP chemically bonded to the surface of the INT and IF (see Fig.1). The second method involved the in-situ synthesis of maghemite NP in the presence of INT and IF. INT and IF were placed in solution with aqueous iron 2+ ions and oxygen ions which then formed NP on the surfaces of the INT and IF (see Fig.2). A dramatic change in the nanomaterial surface charge, i.e. ζ potential, between the starting materials and the products confirmed that the bonds had been formed. Examination under HR-TEM and HR-SEM revealed that both processes had been successful in creating a multilayer maghemite coating on the surface of the INT and IF.

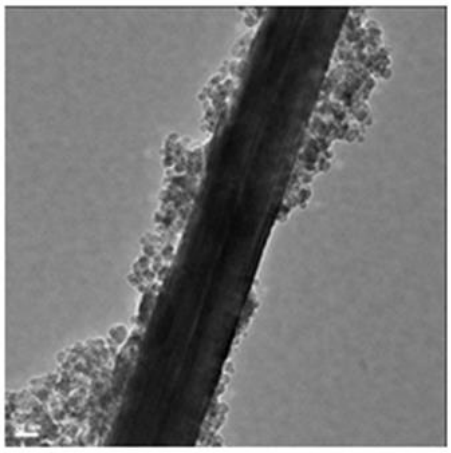

Figure 1: HR-TEM (magnification 200,000x)
WS_2 INT coated with CAN-maghemite NP (Formed by method 1)

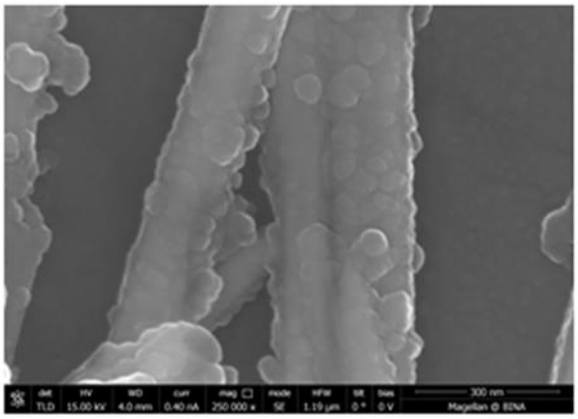

Figure 2: HR-SEM (magnification 250,000x)
Several WS_2 INT coated with maghemite NP (Formed by method 2)

BIOCHEMISTRY :: ALBECK LAB

Talia Felman (Stern College) "The Role of Peptide- and Peptidomimetic-based Cathepsin-C Inhibitors in Inhibition of Necrosis "

Necrosis is a type of cell death that occurs as a result of trauma or internal disturbances in the cell. It often accompanies neurodegenerative disorders, heart disease, neuronal ischemia and toxicity, muscular dystrophy, diabetes, and infections. Unlike apoptosis, necrosis is considered non-programmed, non-controlled, and harmful to the organism. Proteases, such as elastase, are thought to play an essential role in the necrotic process, as they are involved in protein degradation and signaling related to cell death.

Research done by Prof. Ilana Natan of Ben Gurion University and Prof. Amnon Albeck has confirmed that elastase-like proteolytic activity is an active and critical element of the necrotic process. Thus, inhibition of this enzyme can impede necrosis. The focus of the current research was the inhibition of the enzyme cathepsin-C, which activates elastase thereby prompting necrosis.

Six compounds were designed as potential inhibitors of the enzyme cathepsin-C and synthesized (Figures 1 and 2). The structures of the compounds have either peptide or peptidomimetic basis. They mimic the biological functioning of the enzyme's usual substrate so that the enzyme will bind to the inhibitor instead of to its substrate. Of the six inhibitors synthesized in this study, two consist of the sequence glycine - phenylalanine but differ in the reactive functional group on the C-terminus, which can be either a vinyl nitrile or vinyl sulfone (Figure 1). These two are abbreviated GCN and GSO_2. Two inhibitors consists of the non-natural amino acid sarcosine and phenylalanine, and they also differ in their C terminus, which is either vinyl nitrile, making it SCN, or vinyl sulfone, designated SSO_2 (Figure 1). The last two inhibitors consist of reduced glycine and phenylalanine (replacing the native amide bond by aminomethylene functionality) and contain either the vinyl nitrile or vinyl sulfone C-terminus (RACN; reductive amination CN and $RASO_2$; reductive amination SO_2) (Figure 2).

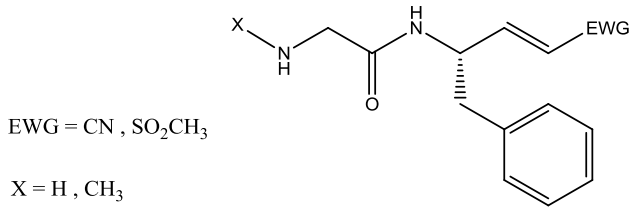

EWG = CN , SO_2CH_3

X = H , CH_3

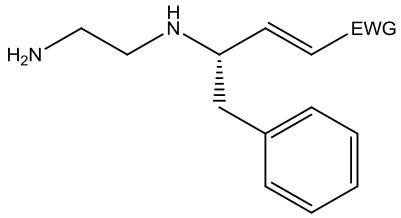

EWG = CN , SO_2CH_3

Figure 1. The structure of GCN, GSO_2 (X=H), **Figure 2.** The structure of RACN and $RASO_2$ and SCN and SSO_2 ($X=CH_3$)

In order to investigate the inhibitors' abilities to prevent necrosis, they were tested on three cell lines. After growing each cell line and incubating them with the inhibitors, KCN was used to induce necrosis. KCN triggers histotoxic hypoxia through the binding of CN^- to the iron ion in cytochrome C oxidase, a complex in the electron transport chain of mitochondria. Thus, aerobic ATP production is disturbed and the cell undergoes necrosis. Following incubation with both inhibitors and KCN, the levels of LDH, a cytoplasmic enzyme released into the medium as a result of necrosis, were recorded in order to determine the number of

ruptured cells. Tomeasure LDH levels in the medium, NADH, a co-substrate of LDH, was added and the product of the reaction was analyzed using spectrophotometry at a wavelength of 340 nm.

The first cells that were studied were PC-12 cells, cancerous cells taken from pheochromocytoma of rat adrenal medulla. The experiment performed on the PC-12 cells consisted of three stages. The first was to test varied concentrations of KCN in order to determine which concentration would most effectively induce necrosis. Concentrations of 20, 15, 10, and 5 mM, and control (0 mM) were tested, and 10 mM was determined to be most appropriate. The second stage aimed to ensure that the synthesized materials would not be toxic to the cells. By incubating the cells with the inhibitors it was confirmed that the cells do not undergo necrosis from the inhibitors or by themselves, but rather, only as a result of the KCN. The last stage included incubating the cells with both KCN and the inhibitors at concentration of 100 μM in order to determine the protective effect of the inhibitors. After completing the experiment and analyzing the results, certain inhibitors proved to be more effective than others (Figure 3). RACN was most protective, decreasing the rate of necrotic cell death by 19%. SSO_2 protected the cells at a level of 14%. GCN protected the cells at a level of 12%.

The second cell line tested was L-6, a less malignant, less aggressively cancerous cell line taken from the skeletal muscle of rats. Using KCN to induce necrosis was not effective and, therefore, the testing of L-6 cells was stopped after the first stage.

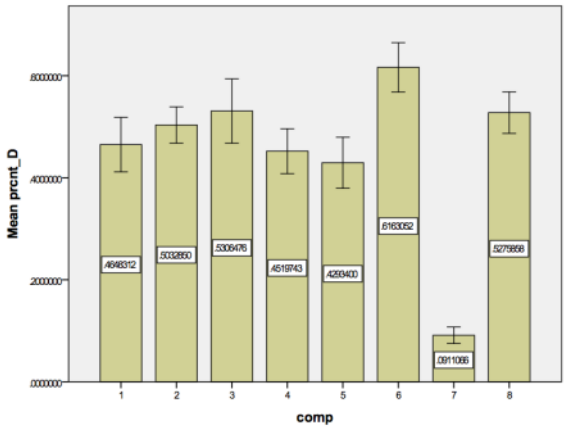

Figure 3. The protective effect of cathepsin C inhibitors against KCN-induced necrosis in PC-12 cells. The inhibitors (left to right): GCN, GSO_2, SCN, SSO_2, RACN, $RASO_2$, control (no KCN), KCN.

The last cell line investigated were the non-cancerous muscle cells of mice in the lab of Prof. Asher Shainberg at Bar Ilan University that were exposed to hypoxic conditions. Due to the non-cancerous nature of these cells, the inhibitors proved to be most protective in this cell line. While not all the inhibitors were equally protective, several stood out as successful. The percent protection relative to untreated cells was as follows: GCN 28%; SSO_2 67%; RACN 63%, $RASO_2$ 33% (Figure 4).

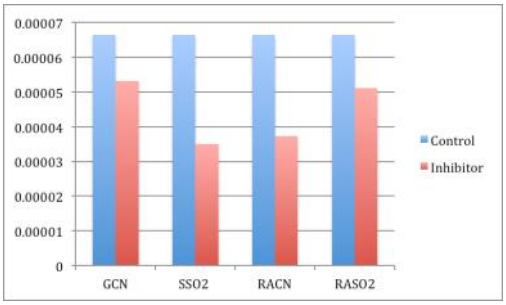

Figure 4. The protective effect of cathepsin C inhibitors against hypoxia-induced necrosis in mouse muscle cells.

In conclusion, this research involved the design and synthesis of six potential cathepsin C inhibitors and evaluation of their protective effect against necrosis. The synthesized inhibitors proved to be effective to varying degrees in different cell lines. The results support the hypothesis of the involvement of the proteolytic enzyme cathepsin C in necrosis.

ORGANIC CHEMISTRY AND NANOTECHNOLOGY :: SUKENIK LAB

Daniel Kaplan (Queens College) "Increasing the Reactivity of Polyethylene sheets using TiO2 and SnO2"

The Sukenik laboratories focus on the synthesis of organic materials that can be easily applied to metal and polymer templates, as well as the development of new technologies to make the templates more reactive. Reactivity is most easily increased by coating the surfaces (metal or polymer) with self-assembled mono-molecular films. This coating allows for the growth of metal oxide thin films on the templates. By developing new technologies for coating these template surfaces, the Sukenik laboratory is developing the ability to coat surfaces that, until now, have been considered impossible to coat due to their limited reactivity.

Over the course of the program I worked with both the organic chemistry and nanotechnology parts of the laboratory. On the organic side we focused on the synthesis of a dithiol starting with 4-hydroxy benzaldehyde. Dithiols are very common organic intermediates as they react well with both aldehydes and ketones. We successfully obtained a dimethylthiocarbonate and worked on the removal of the protecting groups to produce the dithiol. Currently, the de-protection is still under investigation.

In the nanotechnology laboratory we focused on increasing the

reactivity of polyethylene surfaces. We examined the differences in reactivity between coating the polyethylene with TiO_2 and with SnO_2. We also compared the differences in amount of time the coatings were dried in extreme heat before the unidentified chemical coating, known as 'Nycote', was applied. Furthermore, we compared various dilutions of the 'Nycote' coating and their ability to remain intact on the polyethylene surface.

While conclusive results are still pending, our initial results indicate that the longer the metal oxide coating was dried on the polyethylene surface, the more metal oxide that was retained on the surface and thus the more reactive the surface became. However, we also observed that the longer the polyethylene was dried, the more cracks were visible under electron microscopy, which can ultimately lead to more difficulty in applying other coatings, such as the 'Nycote'. Further research aims to determine which metal oxide makes the polyethylene sheets more reactive and also focuses on the strength of the connection between two coated polyethylene sheets which have been glued together.

COMPUTATIONAL CHEMISTRY :: SENDEROWITZ LAB

Sharona Kay (Stern College) "Implementation of Docking Methods in the Stabilization of F508del-CFTR"

Cystic fibrosis (CF) is an autosomal, recessive, lethal disease affecting more than 70,000 people world-wide (~600 in Israel). The disease affects multiple organs and is characterized by chronic pulmonary obstruction, pancreatic enzyme insufficiency, elevated sweat chloride level, and reduced fertility in both male and female patients. CF is caused by mutations in the Cystic Fibrosis Transmembrane Conductance Regulator (CFTR) gene.

The cystic fibrosis transmembrane conductance regulator (CFTR) is a 1,480-residue, multidomain integral membrane glycoprotein localized at the apical membrane of epithelial cells. CFTR belongs to the large superfamily of ATP-binding cassette (ABC) transporters, which are integral membrane proteins that use the energy generated from ATP binding and hydrolysis to translocate a wide variety of molecules across cellular membranes.

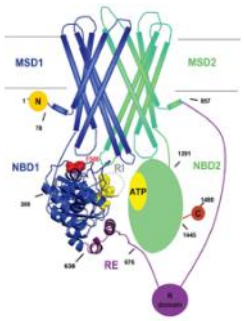

Figure 1. Schematic model of full length CFTR

Cystic Fibrosis is caused by mutations to CFTR. More than 1900 mutations have been identified in CFTR, with different prevalence and symptoms severity and all compromise its ability to conduct chloride ions across cell membranes (Figure 2). Impaired chloride conductance disrupts the ion-liquid balance across the epithelial cells lining the respiratory system, leading to dehydration of the mucus layer lining the lungs and to its colonization by bacteria, ultimately resulting in chronic lung disease and lung failure.

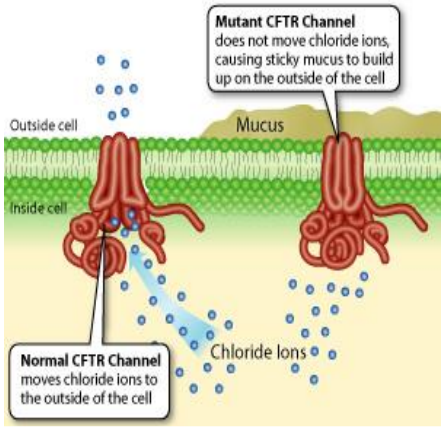

Figure 2. Schematic view of wt and mutant CFTR channel

A remarkable number of CF patients, about 90%, carry at least one copy of a gene with a specific in-frame deletion causing the loss of a single phenylalanine residue at position 508 within NBD1 (one of the two nucleotide binding domains on the CFTR protein) (F508del-NBD1). This mutation in the first NBD almost completely abolishes correct cellular processing of CFTR in CF patients, and consequently most of the mutant protein is incorrectly or incompletely folded and becomes targeted to endoplasmic reticulum-associated degradation (ERAD). On the molecular level, experimental evidence suggests that the F508del mutation reduces the folding efficiency and thermodynamic stability of NBD1 by 6-7°, reducing the protein stability.

Stabilization of F508del-NBD1 partially correlates with rescue of mutant CFTR maturation, folding and function. Potent small ligand which stabilize NBD1 (NBD1 stabilizers) are currently lacking. Thus, discovery and screening of potential ligand binding sites on F508del-NBD1 may lead to the identification of drug-like NBD1 stabilizers that may rescue F508del-CFTR.

This project involved the testing of CDOCKER, a CHARMm-based docking method on the Discovery Studio 3.5 program, in order to determine if the program could be used to screen potential ligands

as stabilizers for F508del-CFTR. Docking is a method which is used to determine the preferred orientation of one molecule when it is bound to another to form a stable complex. In order to test the docking capability and accuracy of the CDOCKER program the ATP molecule was removed and then docked on the F508del-NBD1 in order to determine if the CDOCKER program could reproduce the position of the ligand. These docked positions could then be compared with the original ATP structure and an RMSD value could be found. In docking the F508del-CFTR produced a very large RMSD value and an inaccurate reproduction of the ATP complex. After alignment of F508del-CFTR and the wild type CFTR (lacking mutation), I found that the wild type has a very similar active site as the F508del-CFTR. I therefore could use the wild type CFTR in my docking procedure and found that it produced a good RMSD value and an accurate reproduction of the ATP complex.

Using CDOCKER, I tried to produce a correlation between energy scores and protein denaturation temperature. A lower energy score in CDOCKER implies a more stable complex. These energies should have a negative correlation with the Tm, the temperature at which 50% of the protein is degraded. A higher Tm produced by a ligand in the protein should correspond to a lower energy score produced by docking. In order to see if CDOCKER could produce this correlation, 27 ligands with Tm values were docked into the F508del-CFTR as well as the wild type CFTR protein. A very poor correlation using all 27 ligands was produced (Figures 3 and 4). When omitting 7 outlier ligands, a better correlation between the docking energy values and the Tm was produced using CDOCKER especially for the wild type CFTR and the F508del-CFTR as well (Figures 5 and 6). Though a fairly good correlation was produced, the poor RMSD results of F508del-CFTR bear further scrutiny. Despite this, these correlation results show that CDOCKER could be a viable method in which to screen other ligands in order to stabilize the F508del-CFTR with further research.

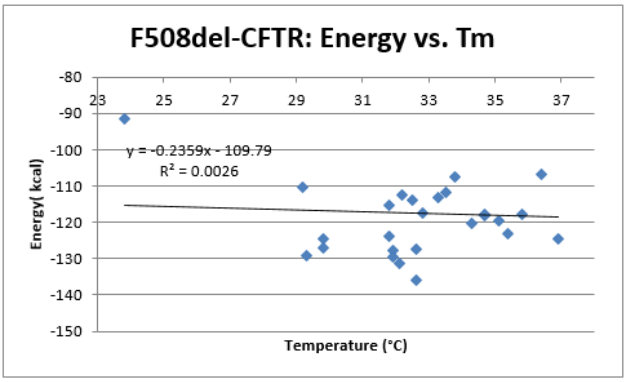

Figure 4. Correlation between docking energy and Tm in F508del-CFTR for all ligands.

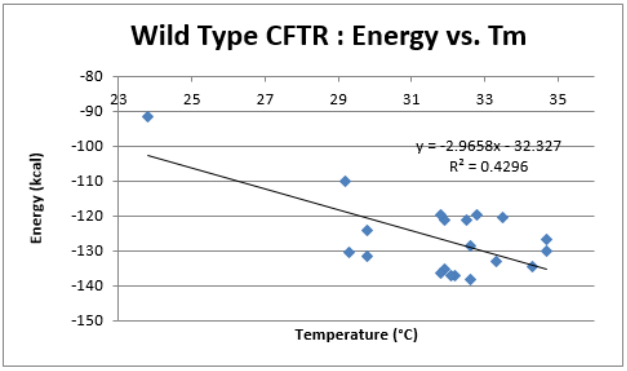

Figure 5. Correlation between docking energy and Tm in Wild type CFTR, omitting 7 ligands.

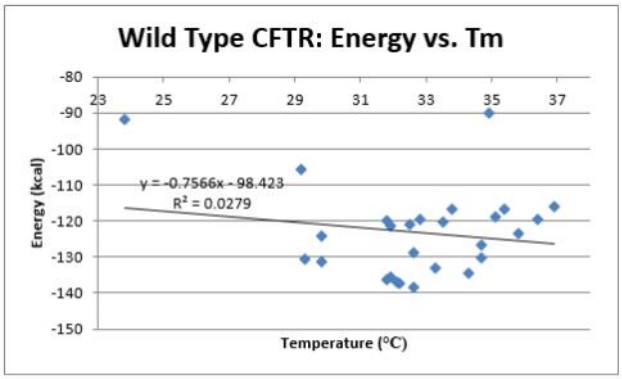

Figure 3. Correlation between docking energy and Tm in Wild type CFTR for all ligands.

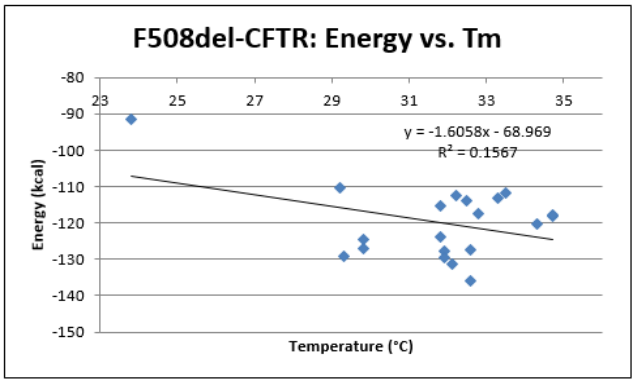

Figure 6. Correlation between docking energy and Tm in F508del-CFTR, omitting 7 ligands.

EXPERIMENTAL PHYSICS AND SUPERCONDUCTORS :: FRYDMAN LAB

Chaim Metzger (Yeshiva College) "Superconductors, Disorder, and the Proximity Effect"

Typically, materials either conduct electricity fairly well while others do not. Substances that conduct electricity well are called conductors. For example copper wiring providing electricity in your homes, and materials, such as rubber or wood, that don't conduct electricity are called insulators. Whether a given material is a conductor or an insulator is determined by how well it conducts electricity, which is conversely known as resistivity. Objects with a high resistivity or resistance are insulators, while those with lower resistance allow for electricity to flow much more easily through them. Unfortunately, even in conductors there still is some resistance, so energy is lost when electric current flows through copper wiring (a conductor).

When certain elements are sufficiently cooled they can become superconductors. This means that the material exhibits zero resistance. Electricity is the flow of charged electrons, and when certain elements are cooled to temperatures approaching absolute zero (-273C), a quantum freeway for electrons and energy to flow without resistance is formed.

It has been experimentally proven that a given element's ability to become a superconductor depends upon the level of disorder in its structure, or structural disorder. A material capable of superconductivity will not be able to superconduct if it is sufficiently disordered.

Even when a potential superconductor's structure is sufficiently disordered it can still become more ordered again by being in the vicinity of another conductor through the "Proximity Effect." The "Proximity Effect" is when one metal or conductor is coupled to a superconducting material and the conductive properties of one material bleed onto the other. Interestingly, the coupled conductor does not need to be able to be superconducting itself in order to turn the disordered potential superconductor in to a proper superconductor.

Our challenge is getting indium oxide to turn from an insulator or limited conductor into a superconductor through evaporation of ultra thin (nanoscale) gold layers which by themselves are not superconductors.

An example of a sample of indium oxide transitioning from insulator to superconductor is shown in figure 1.

For this result we used a special technique called quench condensation for evaporating gold at temperatures near absolute zero (0-12K). By heating the gold we can liquefy and evaporate part of it despite the local temperature being near absolute zero. Beginning with the black line you can see how with each successive nanolayer of gold coating the indium oxide the film crosses over from an insulator to a superconductor. The black line (before gold evaporation) shows the resistance increasing as the temperature decreases towards absolute zero (0K). With each subsequent line representing another application of gold we see that the indium oxide reaches superconductivity represented by the orange line.

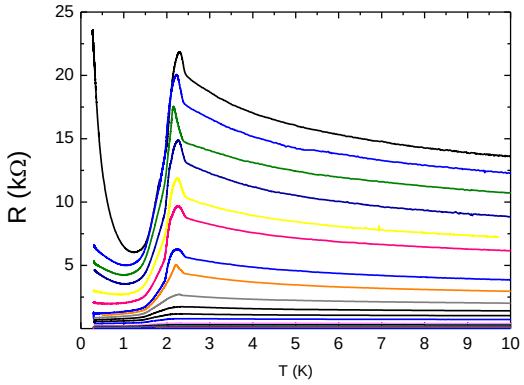

Figure 1 – Resistance versus Temperature for Indium Oxide covered by gold nanolayers

CHEMISTRY AND NANOTECHNOLOGY :: GEDANKEN LAB

Zachary Moldwin (Yeshiva College) "Fabric Sonication with Bactericidal Nanoparticles, and Durability of Fabrics Sonicated with Metal Oxide-Dye Combinations"

As part of Professor Aharon Gedanken's research team, I assisted in a variety of projects involving sonication as a method for attaching nanoparticles to various surfaces. Sonication involves the use of ultrasound irradiation to create bubbles in a solution. Under these conditions, the bubbles undergo an implosive collapse, termed "cavitation," and solute nanoparticles form. "Microjets" of liquid created by cavitation propel these nanoparticles at high speed and pressure, embedding them firmly onto a substrate. The projects I was involved in were antibacterial coating of cotton bandages and antibacterial coating of polyethylene.

The principal reaction under investigation is that of a metal-acetate salt, such as zinc acetate or copper acetate. An aqueous solution of the salt is sonicated, and ammonia is added in order to form an intermediate which eventually converts to a metal oxide. This product is deposited on the substrate by sonication.

Our lab has previously developed a method to produce colored

antibacterial cloth. This involves sonication of the fabric with a combination of dye and nanoparticles. We attempted to find the best dye and nanoparticle candidates in terms of long-term durability. We took samples of various permutations of the two and then put them in a mechanical shaker at a high temperature for seventy-two hour periods, after which we analyzed the original and shaken samples with UV and F(R) spectroscopy, as well as Inductive Coupling Plasma (ICP) analysis and Scanning Electron Microscopy (SEM). We used the data from the shaken and control samples to find the combinations which retained the highest concentration of dyes after shaking.

My second project involved thymol and tannic acid, organic compounds which demonstrated bactericidal properties. We examined of the efficacy of deposition of thymol and tannic acid nanoparticles, respectively, onto polyethylene film and cotton bandages through sonication. This involved performing a series of trials to examine the bactericidal effects of the coated substrates at various concentrations. For thymol, we used increasing quantities of solute in both water and water-ethanol solvents; for tannic acid, we used aqueous solution, along with a tannic acid-zinc acetate mixture. We submitted SEM samples to examine the nanoscale quality of each sonication.

To prepare for my research, I studied the principles of the sonochemical coating method, the preparation of samples for ICP analysis, and the application of UV-spectroscopy in order to determine dye concentration.

• • • • • • • • • • • • • •

ENGINEERING / COMPUTER SCIENCE

Left to right: S. Javitt, M. Levine, E. Zinberg, Y. Mildwid, J. Herzberg, N. SantaCruz, E. Friedman, C. Leibowitz

ROBOTICS AND ARTIFICIAL INTELLIGENCE :: KAMINKA & AGMON LAB

Eli Friedman (Cooper Union) "High Speed Obstacle Avoidance of an Autonomous Micro Aerial Vehicle"

We are participating in the Pearls of Wisdom Micro Aerial Vehicle (MAV) competition in September 2014. The competition requires that a small aerial vehicle weighing less than three kilograms and smaller than one meter navigate autonomously through an obstacle course to a series of waypoints. We present our solution to this challenge.

Our MAV is the AscTec Firefly hexacopter purchased from Ascending Technologies. The hexacopter weighs 2 kg and has a diameter of 0.7 m. It has six brushless motors with 20 cm propellers. Pitch and roll stabilization are accomplished using an onboard Inertial Measurement Unit feeding data to a low level ARM7 processor, which runs a position control system at 1 kHz. A magnetometer, pressure sensor, and GPS are used to receive position information in a global reference frame. A Hokuyo 30 meter planar laser is mounted to the hexacopter for localization and obstacle avoidance. The sensor information is combined in an Extended Kalman Filter (EKF) to achieve a more precise estimate of our location and pose.

The onboard processing is split between the low level processor, which reads the sensor information and outputs the motor commands, and a high level processor, which runs the EKF for state estimation and position control and is used to communicate between the onboard computer and the low level processor.

The main autonomous navigation is done using an onboard Mastermind computer, which has a Core 2 Duo processor and 4GB RAM. The computer runs the Robot Operating System—a collection of software frameworks that are useful for performing robotics tasks.

The competition consists of two missions. The first tests the speed at which the MAVs can fly to waypoints without any obstacles. We implement a bang-bang control system, which quickly accelerates the hexacopter in the direction of the next waypoint and quickly decelerates it when it reaches the waypoint.

The second mission requires the MAVs to fly to waypoints while avoiding obstacles. The challenge lies in the need for the hexacopter to fly quickly, but safely, through the course. We obtain a local map of our environment using the laser scanner and a scan matching library. Since we do not have global knowledge of the map beforehand, we cannot travel the optimal path between our position and the next waypoint. Instead, we select the closest obstacle blocking our path to the goal and plan an optimal trajectory around it. This is done until the goal is reached.

As of this writing, we are in the process of testing this algorithm for speed and safety, while comparing it to other algorithms.

COMPUTER SCIENCE AND FILE COMPRESSION :: KLEIN LAB

Josh Herzberg (Cooper Union) "Enhanced Wavelet trees for Huffman Codes"

Given a file T, and its Huffman encoded text, E(T), a Wavelet tree is a data structure that achieves direct access to T by reordering the bits of E(T) and using additional negligible memory space, resulting in the fact that E(T) is not needed any more. We improve the Wavelet tree for Huffman Codes by suggesting a different reordering of the bits of E(T) and even less negligible memory storage while still supporting direct access to the Huffman encoded file. Furthermore, the suggested data structure reduces the processing time needed for extracting the ith character of T.

Recall that the binary Huffman tree is defined as follows: imagine that every edge pointing to a left child is labeled 0 and every edge pointing to a right child is labeled 1; each node v is associated with the bitstring obtained by concatenating the labels on the edges on the path from the root to v. At each node, v, that is a leaf of the tree, there is a char or word represented by this bitstring. To decode the text using the Huffman tree, one would start at the root, and go to the left or right child (for a 0 or 1, respectively) for each encoded bit until a leaf was reached. The leaf then contains the decoded word. This process can be repeated to decode the entire text.

A Huffman tree is a canonical Huffman tree if, when scanning its leaves from left to right they appear in non-decreasing order of their depth. A Skeleton Huffman tree is a binary tree which is induced by the underlying canonical Huffman tree but which has generally significantly fewer nodes. In a regular Huffman tree the leaves correspond to full codewords. A Skeleton Huffman tree is a canonical Huffman tree from which all full subtrees of depth $h \geq 1$ have been pruned. Thus, each path from the root down to a leaf corresponds to a prefix of a codeword which is necessary in order to identify the length of the current codeword.

Consider for example the alphabet {E, _, A, F, T, H, L, M, N, R, U, V, W} for the string T =HUFFMAN_WAVELET_TREE with occurrences {4, 2, 2, 2, 2, 1, 1, 1, 1, 1, 1, 1, 1}, respectively. The figure depicts the resulting Canonical Huffman tree in which the Skeleton tree nodes are colored in gray. The numbers in the leaves of the Skeleton tree are the lengths of the remaining part of the codeword.

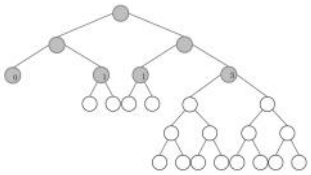

Variable length codes, such as Huffman codes, improve the compression performance. However, random access to the ith codeword of a file encoded by a variable length code is no longer trivial since the beginning position of the ith element depends on the lengths of all the preceding ones.

Implementing rank structure on bit-vectors to develop a data structure called a Wavelet tree allows direct access to any codeword. The Wavelet tree is structured as follows: the root holds the bitmap obtained by concatenating the first bit of each of the sequence of codewords in the order they appear in the compressed text. The left and right children of the root hold, respectively, the bitmaps obtained by concatenating, again in the given order, the second bit of each of the codewords starting with 0, respectively with 1. This process is repeated recursively with the children. To decode the ith codeword, set spot = i and go to spot in the root bitstring, and then go to the appropriate child (0 for left, 1 for right) and set spot = the number of 0s or 1s (depending on the previously found bit), and repeat in for each node until a leaf is reached. In the Skeleton tree, at the leaf the fixed length of the remaining part of each codeword is stored. Using the same example as before, the Skeleton Wavelet tree would look like this:

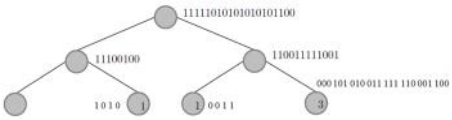

As mentioned, in order to access the ith codeword in the Wavelet tree, the number of previous 1s (or 0s) has to be known at each node along the path. This can be done by counting the 1s (or 0s), until the desired spot, but that will take linear time. Instead the rank structure is use as follows: if n is the length of a bitstring, the rank structure saves the rank of every log2(n) bits (called meta level), and then saves the rank of every log(n)/2 bits (called sub level) relative to each meta level, and, finally, uses a table to determine the rank relative to the sub level. The rank structure finds the rank of the ith bit in constant time, while using only a little extra memory. Additionally, this result is significantly enhanced using the Skeleton tree, instead of a Canonical tree.

ADVANCED MATERIALS AND NANOTECHNOLOGY :: NAVEH LAB

Shoshana Javitt (University of Maryland) "Exfoliating Molybdenum Disulfide on a Self-Assembled Monolayer "

Graphene is a material composed of pure carbon and is one atom thick. It is nearly two dimensional and close to transparent but it is quite strong and a highly conductive material for heat and electricity. The material's properties are important for the advancement of electronics, manufacturing smaller electronic devices, and many other technologies. One of the current methods for producing a monolayer of graphene is Mechanical Exfoliation using adhesive tape.

Molybdenum Disulfide (MoS2) has similar properties to graphene; it is very thin, transparent, and flexible. But one of the distinct properties of MoS2 which makes it different from graphene is that it has a wide band-gap. This property is very important for use in building transistors and logic circuits. Just like graphene, MoS2 can be mechanically exfoliated using tape. Since the van der Waals forces connecting the layers are not very strong, the layers are easily separated. In the exfoliation process, a crystal of MoS2 is put on the tape and then the tape is used to separate the flakes into thinner layers. The flakes are then stuck to a Silicon Oxide (SiO2) wafer. Normally, atomically thin MoS2 flakes are transparent. However, when placed on SiO2, the MoS2 layer interacts with light and changes the color in a way that enables the eye to distinguish between the MoS2 flakes and SiO2 substrate. The reflected light also causes a visual difference between thicker and thinner layers so that it is possible to see which flakes are monolayers. The problem with this method is that the SiO2 interferes with the properties of MoS2. Oxide has a lot of charged impurities stemming from dangling on the SiO2 surface. Calculations and experiments show that these defects on the substrate change the behavior of MoS2 and affect its electrical characteristics.

Therefore, we are looking for a way to reduce the changes to the MoS2 during the exfoliation process so that it retains its electrical properties. We coated the SiO2 surface with a self-assembled monolayer (SAM) of Octadecyltrichlorosilane (OTS). This monolayer is intended to isolate the MoS2 from the oxide's charge impurities. OTS also creates a smooth surface and is easy to use to coat SiO2. Also, since OTS has a hydrophobic surface, the adhesive should not be attracted to it; this should greatly diminish the amount of adhesive seen on the chip.

Exfoliation was done both on a pure SiO2 surface and on a surface with a monolayer of OTS on top of the SiO2. In Fig. 1 a lot of adhesive can be seen on the regular SiO2 surface. However, Fig. 2 shows almost no adhesive on the OTS surface.

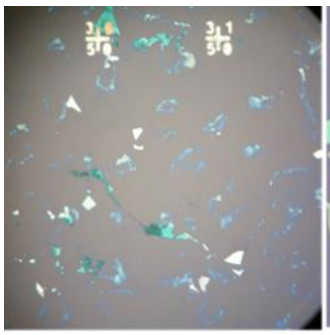

Figure 1: Optical image of MoS_2 exfoliation on silicon oxide.

Figure 2: Optical image of MoS_2 exfoliation on a monolayer of OTS.

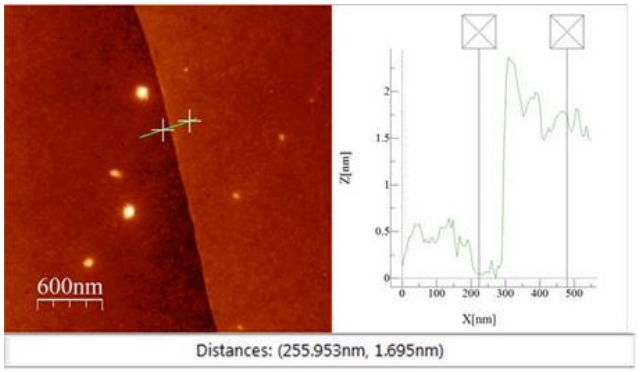

Figure 3. AFM Image.

The few-layer thick flakes of MoS2 were analyzed using AFM, Atomic Force microscopy, and RAMAN spectroscopy to determine the exact thickness of the flakes. The AFM test determined that one flake of MoS2 on the OTS coated sample is about 1.7 nm thick, which is a bilayer (Fig 3).

Electrical Characterization needs to be done on this flake in order to determine the effect of OTS on the MoS2. These tests and characterizations will determine if OTS improves the electrical properties of exfoliated MoS2 in comparison to exfoliation done on pure SiO2.

MACHINE LEARNING :: KOPPEL LAB

Caleb Leibowitz (Cooper Union) "Determination of the Number of Authors of a Multi-Author Document"

The problem of decomposing multi-author texts by distinct authorial threads is known to be solved, assuming the number of authors *k* is known. However, estimating the number of authors in a multiple-author document remained an open problem. We present a novel supervised method to estimate the number of authors in a multiple-author document. We do this by merging an

imposter document, written by a single author, with the document we wish to analyze. We then perform decomposition on the new merged document and measure the performance of the decomposition on the imposter document. Since document decomposition is not robust with respect to k, we can choose the optimal *k* as the *k* which leads to the best decomposition of the imposter document. The number of authors of the original document is then estimated to be *k* – 1.

COMPUTER SCIENCE AND COMPUTER GRAPHICS :: WEBER LAB

Michelle Levine (Stern College) "The Deformation of 3D Images Using Moving Least Squares and the Complex P2P Cauchy-Green Method"

The goal of this research is to create an efficient algorithm to deform images while maintaining a realistic picture. An image can be transformed by setting a mathematical path for each vertex from its original position to the new deformed location. Simple transformations include translation, scaling, and rotation in 2D and 3D polygons. Translation is when the image is shifted, but all points, angles, and lines remain the same relative to each other. It moves every point a constant distance in a specified direction. Scaling entails enlarging or shrinking an image, while leaving angles the same but extending lines or points in a quantified direction. The 3rd type, rotation, provides a specific map in which everything in the image moves around a designated axis or point.

In this particular project, we are trying to find an effective way to transform an image by moving a vertex and simultaneously mapping paths for the surrounding vertices. One method that has been developed is to deform images using Moving Least Squares. In this technique, the paths of the vertices are determined by continuous functions, which are calculated by a weighted least squares quantity. The points surrounding the chosen vertex are more greatly affected than those farther away from the focus.

Three classes of linear functions used in MLS (Moving Least Squares) deformations are affine, similarity, and rigid transformations. Affine transformations have a linear transformation followed by a translation: Ax + b (Matrix A, vector b). The issue with this class is that the transformation often results in non-uniform scaling, causing the image to lose its realistic nature. In similarity transformations, only translation, rotation, and uniform scaling are allowed. These restrictions are established by constraining the matrix M to follow MTM = λ2I for some scalar λ. Similarity transformations better preserve the angles between points, as compared to the general affine deformations, but still allow for scaling in undesirable areas. This leads us to rigid deformations in which angles are maintained and even uniform scaling is not allowed. The matrix M, in this class, is constrained to MTM = I, and

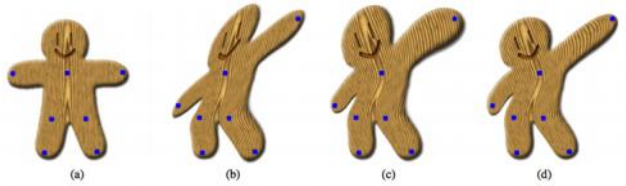

Figure 1: Deformation using Moving Least Squares. Original image with control points shown in blue (a). Moving Least Squares deformations using affine transformations (b), similarity transformations (c) and rigid transformations (d).

the mathematical function is altered accordingly. The deformation now preserves rigidity and scale locally so that the relative shape of the original image is retained. The differences in each of these classes are shown in the images below, where in (b), the general affine transformation causes non-uniform scaling in the arms and torso, in (c), the similarity transformation scales the size of the arm as it is stretched, and in (d), the rigid transformation provides a more realistic deformation. These methods can also be extended to using line segments as the focus point, rather than sets of points.

The issue with these methods of deformation is that the weighted Moving Least Squares calculation determines the affect on other points based on proximity to the requested point, without taking into account the borders of the image. This causes issues when there are two vertices in close proximity with each other but separated by a border. The 2nd vertex will have a larger deformation than intended, causing an unrealistic and warped result. Professor Weber and his colleagues came up with the P2P Cauchy-Green method in which the borders of the image are calculated and the points are then weighted within those boundaries. The difference between the two methods is shown clearly in the left image below, in which the MLS deformation causes a warped result in the frog's knee, while the P2P method effectively separates the vertices based on the image border. In the image on the right, the border restricts the coordinates of the point and the effects on the surrounding region in P2P, but in MLS, the effect spills over into the nearby knee. The ongoing research focuses on potentially using complex numbers in order to weigh the proximity of the surrounding vertices.

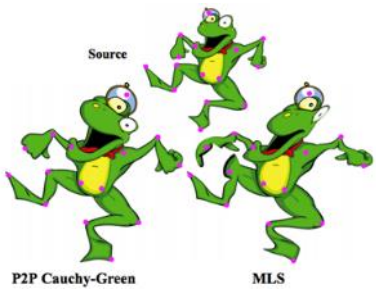

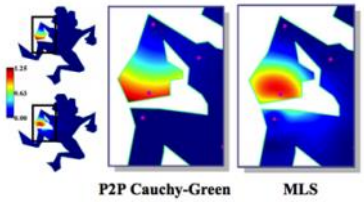

Figure 13: *Absolute value of the P2P and MLS coordinates of the point on the left hand. The MLS coordinate "spills" into the leg near it, whereas the P2P coordinate does not.*

In order to test these deformations, we use the Maya 3D animation software to create 2D and 3D images, which we can then manipulate using the commands already installed within the software. However, another aspect of the research has been in coding Maya plugins, extensions for the animation software, in C++, Maya API, and MATLAB. In my project, I wrote code for the ColorMeshVerticesCmd that creates two empty color sets; the Valence Color Set arranges the color of the polygon based on the number of connected vertices for each vertex, while the Gaussian Curvature Color Set adjusts the colors based on the Gaussian curvature of each vertex. The Gaussian curvature is determined by subtracting the sum of the angles of the adjacent triangles from either 2 pi (for a non-boundary vertex) or pi (for a boundary vertex). This command is performed on a polygon that has a triangular mesh, meaning that the image is broken down into a set of triangles on all faces. The last part of the project was to create the InverseMatrixCmd. The matrix is created in C++ using the GMM Library and then inverted using MATLAB-Maya interface code.

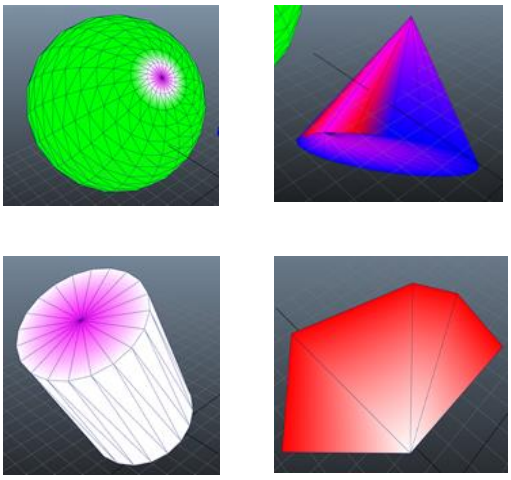

BIOENGINEERING :: WEISS LAB

Yaron Milwid (University of Toronto) "Developing a Work-flow For Analyzing Telomere Images"

Telomeres are repetitive nucleotide sequences at the ends of chromosomes whose length has been proposed as a biomarker for certain pathologies or aging. This project concerned the measurement of relative telomere length and telomere count within human lymphocytes. The data analyzed in this work were derived from images obtained using fluorescence microscopy with the DNA stained using DAPI and the telomeres labeled with a PNA (protein nucleic acid) marker. The slides were prepared in the laboratory of Dr. Aliza Amiel (Meir Hospital, Kfar Saba, Israel) and imaged using a fully automated Nikon TE2000 microscope (60X/NA=1.4 objective) by Ms. Batya Mennasse-Green and Ms. Hila Kilze.

The raw data consisted of the DAPI images that showed the nuclei, and the PNA labeled telomere image stacks (Figure 1). Generally, 20-40 fields were acquired, providing a total of 150-250 cells/slide. Theoretically, each cell should contain 92-184 telomeres, depending on its stage in the cell cycle (46 chromosomes x 2 ends/chromosome = 92; cells entering mitosis would have double this number). The data included 25 slides, or about 3750—6250 cells. The parameters of interest include telomere intensity, which is expected to correlate with telomere length, and telomere count (Figure 1).

In order to process this large quantity of data, a set of image processing tools was developed, using the Fiji distribution of ImageJ. An additional tool for processing the output of the image processing steps was developed using Python (version 2.7), and statistical analysis was performed using R. Figure 2 shows the workflow for the data analysis. These steps are described in Figure 2.

Segmentation of the nuclei:

The nuclei were detected using an automatic thresholding method (either the maximum entropy or Huang method). The objects were dilated, but not merged, in order to detect telomeres on the periphery of the nuclei. The output of this step was a set of regions of interest (ROI) that uniquely identified each nucleus. Conditions on size and roundness were used to filter the detected objects. Figure 3 shows the segmentation as applied to the image of Figure 1.

Telomere detection:

The telomere detection script iterates over each nucleus, and detects the telomeres using the detect maxima function of Fiji. The noise threshold and telomere size limits are user selectable, and the size limits were used to filter the output of the detect maxima operation. This script produces a unique data file for each cell, in

addition to a number of summary files that enable the user to see an overview of the output and visually check the detection quality.

Listing and editing of the detected nuclei:

A standalone Python script creates a file that contains a listing of all individual nuclei data files for a given slide. This file, the nuclei image stack, and a complete nuclei ROI set, are the inputs to a Fiji script that allows the user to interactively edit the detected nuclei and remove false positives. False negatives are not added, because the nuclei segmentation program detects more than enough nuclei for our purposes. The output of this step is an edited listing file, which will be used in the next step. Figure 3 shows an example of an image in which a nucleus has been edited out.

Processing of the nuclei data:

A standalone Python script analyzes all of the individual nucleus data files that appear in the listing file (produced by the previous step). This script produces a set of parameters for each cell and writes them to a single line in a summary file. Thus, 100-200 nuclei (and files) are reduced to a single summary file. Table 1 lists the parameters currently provided. It is not difficult to modify or add parameters as needed. These summary files are used as input to R, for further statistical analysis.

Discussion:

High volume microscopy datasets are often extremely large and difficult to interpret. In this project, thousands of cells were imaged, producing about 120GB of image data. Automated tools for the processing of these data must be developed in order to process these large datasets.

Here, we presented a set of tools to do that. The tools include automated object detection and data compression, addressing two different challenges. Automated object detection presents the challenge of how to accurately segment images in the presence of noise and artifacts. In this case, our tools detect all potential nuclei, while inserting an interactive editing step to remove false positives. This represents a balance between the computer's strength (speed) and the human's strength (global analysis). The data compression step reduced the data size by a factor of about 200. The challenge in data compression is to decide which parameters are significant. Statistical analysis (eg using R) must be used to decide which parameters are significant. This can be fed back into the processing script as needed.

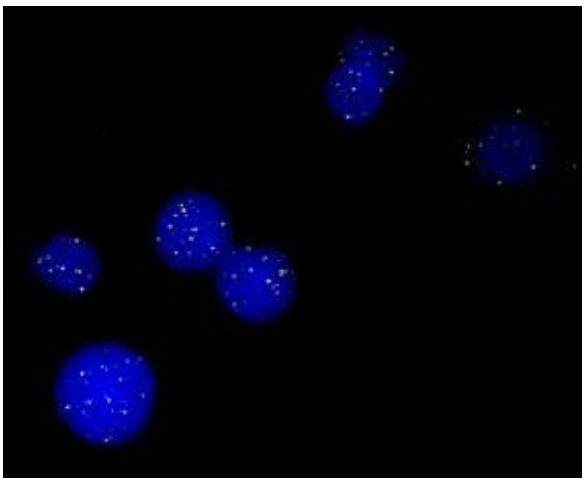

Figure 1. Telomere image (yellow) overlayed on DAPI image (blue). Contrast has been stretched to improve visibility.

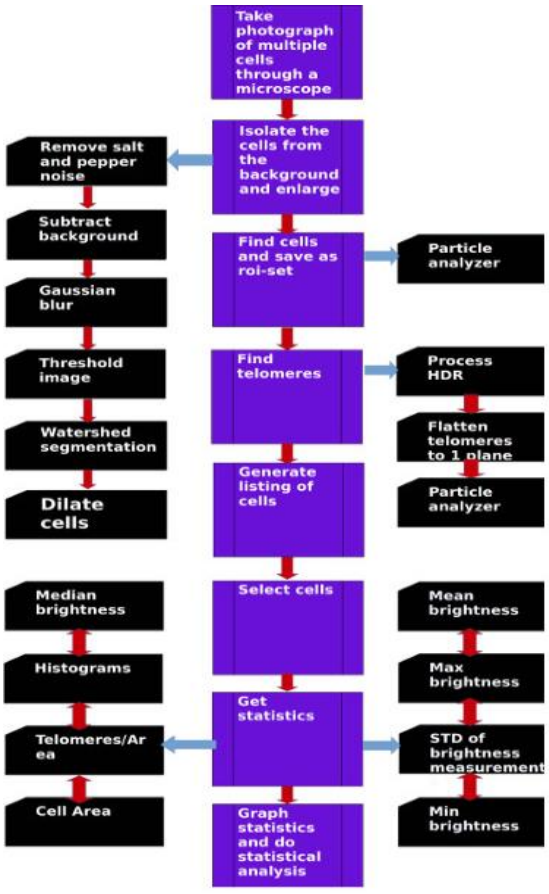

Figure 2. Workflow of analysis of telomere images

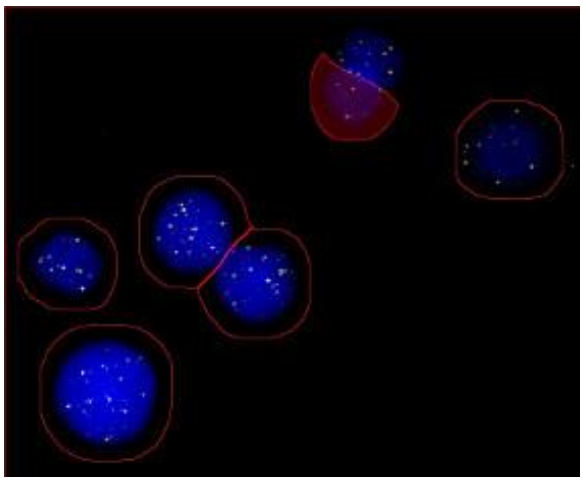

Figure 3. Nucleus detection, shown as red overlay. The "split" object actually derived from two overlapping objects that were split with a watershed operator. The split object is overlaid in red, following deletion with the nuclei editing tool.

Telomere count
Mean telomere brightness
Histogram of telomere brightness
Max telomere brightness
% of telomeres above 50% brightness
PDF of telomere brightness
CDF of telomere brightness

Table 1. Examples of outputs from data analysis code

SIGNAL PROCESSING :: BERGEL LAB

Noah Santacruz (Cooper Union) "Nearest in Cone Routing in Wireless Adhoc Networks "

As wireless-enabled devices proliferate, so do wireless adhoc networks (WANETs). These networks are made up of many mobile devices, known as nodes, which can each connect to any other node in the network. This type of network is advantageous because it requires no existing infrastructure to setup. It also allows multiple users to share one user's internet connection. However, it is more complicated to send messages in this network because the interference and noise the message will experience can be unpredictable.

Interference is when another message crosses the path of the transmitted message, causing a distortion in the received message. Noise is caused by environmental factors, which become more acute the farther the message has to travel. While these two factors are normally an issue for any type of communication, they are especially problematic in WANETs, because these networks tend to be dense. To overcome these problems, it is common to route the messages in the network by hopping from node to node until the message reaches its final destination. The risk of any given link failing is far less than the risk of an end-to-end transmission failing, because the distance is much shorter.

The challenge this lab dealt with was to study several known algorithms for routing in WANETs and testing their effectiveness. To be considered, an algorithm needed to be able to work using only local knowledge available to a computer in the network, because, unlike in traditional networks, there is no central controlling router. Also, the algorithm needed to be computationally simple, so as to be able to run on any mobile device without drawing too much power. It was this student's job to measure the performance of the Nearest in Cone (NiC) algorithm.

The figure 1 depicts this algorithm. In it, θj is the angle between the jth transmitter and the final destination, Φj is the angle of the maximum possible variation from θj and ψi,j the angle between the jth node and the ith node. The nearest node in the cone $(\theta j - \Phi j/2) < \psi i,j < (\theta j + \Phi j/2)$ is selected as the next node to hop to, because it is considered within the general direction of the final destination.

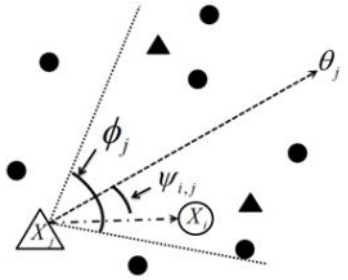

Figure 1.

Using Matlab, a simulation for the NiC algorithm was created and used to analyze its performance. From the data gathered, it was determined that certain nodes were far more likely to be chosen as relays in a message path, depending on their position in the network. Because of this, these nodes effectively became bottlenecks, limiting the overall success of messages. See figure 2. The pink spots represent nodes. The redder a node, the more times it was chosen as a NiC. It was shown that the number of messages received at each node was almost inversely proportional to the NiC count even though these nodes should have had increased traffic. See figure 3; r

redder nodes received more messages. This was caused by an increased likelihood in seeing interference in messages sent to these nodes because of their location in the network. In the future, the lab will optimize the network parameters to account for this.

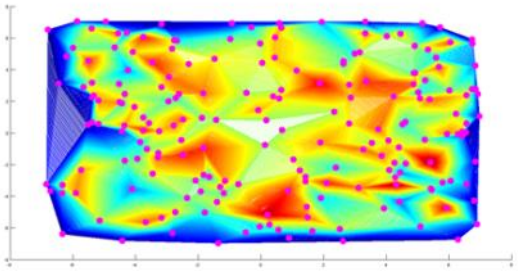

Figure 2.

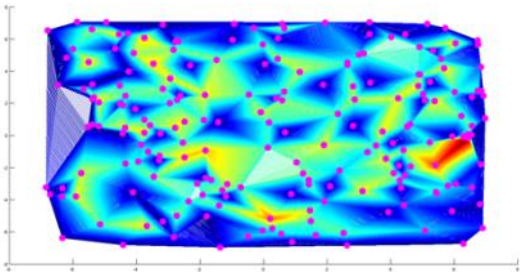

Figure 3 .

CRYPTOGRAPHY :: HAZAY LAB

Eitan Zinberg (Yeshiva College) "Designing Provably Secure Protocols for Secure Two-Party Computation in the Presence of a Semi-Honest Adversary "

Secure multiparty computation enables a number of distinct parties to carry out a joint computation of some function, called distributed computing, in a secure environment. Secure multiparty computation has many applications, ranging from a simple coin toss to electronic voting and auctions. We are specifically concerned with the possibility that an adversarial entity controls a subset of the parties and wishes to attack the protocol execution. The two main requirements of a secure computation protocol are privacy and correctness. Privacy requires that parties not learn anything other than their own output, as nothing else is necessary for them to learn. Correctness means that each party should receive its correct output.

According to the standard definition today, a protocol is considered secure if it meets the ideal/real simulation security definition. In an "ideal world," an external trusted party carries out the computation. The parties simply send their inputs to this party and receive their output of the computation. In the "real world," however, there is no external trusted party. The parties run the protocol among themselves. In order to be considered secure, the real protocol execution must mimic an execution in the real world. Namely, an adversary in a real world execution should not be able to do any more harm than in an ideal world. More formally, security of a protocol is established by comparing the outputs of the adversary and honest parties in a real protocol execution to their outputs in an ideal computation.

There are several different models for adversaries that assume different strengths and corruption strategies. Specifically, static corruptions imply that the adversary cannot corrupt additional parties during the computation, whereas adaptive corruptions can take place anytime during the protocol execution, even after it is completed. In addition, the adversary can be limited to running in polynomial time or be computationally unbounded. There are also different allowed adversarial behaviors. In the semi-honest model, the corrupted parties still follow the protocol specifications correctly. However, the adversary attempts to learn information from the internal states of the corrupted parties. In the malicious adversarial model, the corrupted parties can arbitrarily deviate from the protocol specification according to the adversary's instructions.

We focused on the simpler two-party semi-honest adversarial model where correctness is not needed to be enforced and only privacy is proven. One protocol that was designed for secure two-party computation in the presence of semi-honest adversaries was a protocol to securely compute the intersection of two private datasets. This was done using a homomorphic encryption called the Paillier Encryption Scheme. This scheme enables a party to perform computations on a ciphertext that on decryption has the result of performing operations on the plaintext. The protocol must then be formally proven to be secure by showing that it meets the ideal/real simulation paradigm. This is done by separately considering the case where the first party is corrupted and the case where the second party is corrupted and ensuring that in neither case does either party learn more than it would in the ideal world.

LIFE SCIENCES

Left to Right: J. Azar, Y. Chen, D. Edelman, A. Straus, J. Farkas, S. Lis, A. Muskat, M. Schechter, J. Grossman, T. Wasserman, A. Wakschlag,

MOLECULAR BIOLOGY :: BEN-AROYYA LAB

Joshua Azar (Yeshiva College) "BRE1's EFFECT ON PSG FORMATION "

Protein homeostasis or proteostasis is essential for the maintenance of regular bodily functions. Misfolded proteins cause the protein to lose its functionality, to become toxic, and can damage other proteins that operate in the near vicinity. Many neurodegenerative diseases, including Alzheimer's and Parkinson's have been linked to misfolded proteins and aggregates. Cells therefore have evolved to rely on a number of different protein quality control (PQC) pathways to prevent protein aggregation and target terminally misfolded proteins to degradation. In eukaryotes, the ubiquitin proteasome system (UPS) plays a major role in PQC by selectively marking and targeting proteins for degradation.

The UPS regulates proteins through a pathway known as ubiquitination. Ubiquitination consists of labeling a protein with polyubiquitin chains which marks that specific protein for degradation in the proteasome. The 26S proteasome is a multisubunit protease that is highly enriched in the nucleus and is responsible for degrading a large number of potentially harmful proteins. The proteasome consists of a 20S core particle and two 19S regulatory particles. Ubiquitinated proteins are unfolded as they are fed down the 19S shaft and are then translocated to the 20S core particle where the protease activity breaks down the protein into short peptide molecules.

Recently it has been discovered that upon carbon source deletion proteasomes are stored in Proteasome storage granule (PSGs), where they can be quickly and efficiently prepared for use when the need arises. Proteasome activity has never been seen within these PSGs and it is unclear whether they are functional and if they are not functional what exactly is keeping them inactive. Much of the current research in the lab is focused on understanding the mechanics and role of these PSGs.

BRE1 an E3 ligase has been recently implicated in the lab as a factor in the relocalization of the proteasomes into PSGs. BRE1 is known to ubiquitinate the lysine at the 123rd position on the histone on H2B (k123) and without BRE1proteasomes will not go into PSGs. However it is unclear whether the ubiquitination of H2B k123 is a factor in the formation of PSGs or perhaps BRE1 causes the formation of PSGs through a passage not involving H2B ubiquitination. Using The baker yeast Saccharomyces Cerevisiae as a model system To determine BRE1's effect on PSGs we created 3 different strains. One wild type strain which has RPN5, a proteasome subunit marked with GFP. In this strain the proteasome should go to PSGs when carbon levels are low. A second strain consisted of RPN5-GFP but with a deletion of BRE1, which prevents the formation of PSGs. A third strain contains RPN5-GFP and mutated k123 in H2B so it can be seen whether PSGs will form when there is a valid copy of BRE1 but without the lysine which is ubiquitinated on H2B-(k123). As of this printing the strains have been created and we hope to run the experiments soon.

Experiments were done under the supervision of Lee Peters and Ofri Karmon of Professor Shay Ben-Arroya's lab.

GENE EXPRESSION :: SHAV-TAL LAB

Yaacov Chein (Yeshiva College) "The effect of Wnt-3a on β-catenin in relation to the CCND1 gene "

β-catenin is a cadherin-associated protein and it is a cofactor in activating the cyclin D1 gene, CCND1. When β-catenin binds to TCF4 in the nucleus it forms a complex, which sits on the CCND1 promoter and activates the gene. Overexpression of β-catenin is associated with many cancers.

Using a fluorescent live cell microscope Professor Shav-Tal's lab determined the kinematics and dynamics of β-catenin in the cell. This was done by creating a time-lapse video using live cell microscopy.

Wnt-3a causes β-catenin to traverse the nuclear membrane and enter the nucleus. Therefore we wanted to determine the effects of Wnt-3a on the kinematics and dynamics of β-catenin. Thus immunofluorescence and live cell imaging were performed on YFP-β-catenin. YFP-β-catenin is β-catenin tagged with a yellow fluorescent protein, which allows for its observation using microscopy. The data collected indicated that the YFP-β-catenin acted similarly to the endogenous β-catenin before and after Wnt-3a was added.

When this experiment was carried out again different results were obtained. At times, the β-catenin entered the nucleus and was exported over time. Other times the time-lapse video showed that the β-catenin entered and left the nucleus repeatedly. We want to determine why β-catenin is acting differently in these experiments. It may be based on what stage in the cell cycle the cells are when β-catenin enters. To investigate this possibility we used a plasmid, which expresses different colors depending the current stage in the cell cycle. Therefore when the cells are in G1 they will express one color and when they are in G2 they will express a different color. To test this, we set up a time-lapse video and depending on the results further experimentation may be necessary.

When the Wnt-3a was added to the YFP-β-catenin there was an aggregation of β-catenin in an organelle right outside the nucleus. Based on the size of the organelle we assumed it was the centrosome, which is the main microtubule-organizing center in the cell. To determine if it actually is the centrosome we performed immunofluorescence with two antibodies. The first antibody, anti-pericentrin, binds to the target molecule, pericentrin, in the centrosome. The second antibody, which has a Cy5 fluorophore, binds to the anti-pericentrin so it can be seen with fluorescence microscopy. The nuclei of the cells were also stained with Hoechst. Using different filters in the microscope we were able to observe and take pictures of what was occurring. The YFP filter showed us the β-catenin, and the Cy5 filter showed us the protein pericentrin, which is in the centrosome. When the pictures from the different filters were compared, it was determined that the β-catenin and pericentrin were overlapping, indicating that β-catenin is found in the centrosome. Also this aggregation sat right outside the nucleus, as seen from the Hoechst staining, which fits with where the centrosome is located in a cell.

We then inserted two genes into Hek 293 cells through transfection. The first gene is YFP-β-catenin and the second is the CCND1 gene tagged with MS2. These genes will be incorporated into the cells' genome and the mRNA that is produced will include the MS2. Now we can use a coating protein for the MS2, which will bind to the MS2 repeats. This will allow us to see the location of the transcription site and the location of the mRNA in the nucleus. However, we cannot use GFP-MS2 as the coating protein since the wavelength used to view it is too similar to the wavelength used to view β-catenin. Therefore we are testing four new genes to determine which will work best with our investigation.

When lithium chloride was added to the cells, we observed that the β-catenin was retained in the nucleus. Thus, we wanted to determine whether Wnt-3a or LiCl was better suited for the retention of β-catenin in the nucleus. Also we want to figure out what is the difference between their mechanisms of action. Before we were able to test which is better, we first had to determine what is the best source of Wnt-3a. We had three different sources of Wnt-3a and we tested each one for levels of β-catenin. We were able to determine the effectiveness of Wnt-3a based on the levels of β-catenin in the cell. The more β-catenin, the more effective the Wnt-3a. Consequently we determined the best source for Wnt-3a, and we are now testing if LiCl works better than Wnt-3a.

Another project we've been working on is with FRAP, fluorescent recovery after photobleaching. This machine allows us to direct a laser at specific particles in a cell, which causes the fluorescent lifetime of those molecules to elapse. The image of the cell now contains a dark spot in the place where the laser was directed. The rest of the fluorescent molecules will now diffuse back to this region, which allows for the determination of the rates of these molecules. We performed FRAP on YFP-β-catenin before and after lithium chloride was added and are now measuring the dynamics and kinematics of YFP-β-catenin.

WILDLIFE HORMONES AND BEHAVIORAL ECOLOGY :: KOREN LAB

Dani Edelman (Yeshiva College) "Hormone Extraction from Hair Samples"

Until recently, levels of cortisol, a glucocorticoid stress hormone, and testosterone were measured in both humans and animals by analyzing blood, urine and saliva samples. There are several limitations with this methodology. Results only show the hormone levels at the moment of sample extraction without the ability to measure variations over time. Cortisol levels can be greatly affected by the acute stress resulting from the invasive procedure of taking the blood urine and saliva, thereby giving inaccurate readings. These samples are often difficult to obtain and need to be transported in specific conditions (i.e. frozen or cold). These methods also incur considerable risk of infection of the subject.

Recently, new enzyme immunoassay (EIA) kits have been developed enabling hormone analysis from hair samples. As hair grows, hormones are deposited into the hair shaft. This acts as a biomarker indicating long-term activity of the hypothalamic-pituitary adrinocortical (HPA) axis. The hair samples can either be analyzed whole, giving average hormone levels secreted during the life of the sample, or segmented to analyze the hormone levels over a specific time period of hair growth. This method is also noninvasive and samples can be stored at room temperature. The application of these new EIA kits, however, has been limited due to their recent development.

Because human hair grows approximately 1 centimeter per month, information about past events can be learned. Samples were analyzed using the new EIA kits for cortisol and testosterone levels. Similar experiments were conducted with hyraxes, *Procavia capensis* and nutrias, *Myocastor coypus*.

COMPUTATIVE IMMUNOLOGY :: MEHR LAB

Jason Farkas (Queens College) "Finding Motifs of Point Mutations in Human B cell DNA ."

In order to fend off specific infections via creating antibodies that recognize particular foreign antigens, two methods are used by the immune system to produce diversified antibodies. Somatic recombination of the germline variable, diversity, and joining gene segments, also termed VDJ recombination, is the first method that leads to the multiple combinations within the assembly of the antigen receptor genes. The second method includes many different pathways and mechanisms to induce genetic mutations that change the DNA base pairs themselves. Once a B cell's antibodies encounters an antigen, a process is triggered wherein genetic mutations within the antibody-coding region are induced. This occurs as the cell divides, creating many clones with slightly different antibodies. This process is repeated for each cell that contains an antibody that fits well with the antigen, until eventually both plasma cells and memory B cells are generated. Memory cells have a very long lifespan and a great antigen- antibody fit. If the body is once again infect by this pathogen, the memory B cells, which are already equipped with the required specific antibody, can rapidly proliferate. This enables the body to produce a much faster and stronger immune response.

Research into how exactly the entire process works is extremely important for many different areas of health. Significant application include understanding autoimmune diseases and developing effective treatments, improving the immune response of the elderly, and creating medicines and treatments that take into account the workings of a specific individuals immune system's health.

The lab has worked on discovering various patterns and motifs in immune cell DNA before and I continued on this research with a new take on approach the data and a focus on DNA that underwent point mutations. I looked at different data sets from both young and old patients and created programs in python to analyze the sequences. This provided a tremendous amount of data which I then worked to condense. First I made a program combine similar datasets and determine statistical values such as the average and standard deviation. I then used statistical modeling to determine relevant data and had a program use that information to determine biologically relevant patterns. The patterns we found are indicative of important motifs that can help shed light on the mechanisms through which these point mutations are induced, but more analysis will be required before anything certain can be said.

VIROLOGY AND MOLECULAR BIOLOGY:: GOLDSTEIN LAB

Jennifer Grossman (Stern College) "The Innate Antiviral Response of HEK 293 Cells to VZV "

The varicella-zoster virus, commonly referred to as VZV, enters the human body through inhalation. Once this virus enters its host, it infects lymphocytes, primarily in the tonsils, that carry it to the skin, where it causes a lysogenic (productive) infection in the form of lesions (chickenpox). The virus also infects sensory and sympathetic ganglion neurons, either via transport from the skin lesions or via infected lymphocytes. VZV remains latent in these peripheral neurons for many years. Often, stress causes the virus to reactivate, resulting in a lytic infection in the form of shingles, a debilitating and painful condition.

The exact method of the establishment of latency in neuronal cells remains elusive. However, Dr. Goldstein's lab at Bar-Ilan has

found (unpublished) that when human embryonic kidney 293 cells (HEK 293) are infected with VZV, the virus enters but does not elicit a productive infection and its genome remains resident, which may serve as a model for latency in an easily grown and genetically modified cell line. PML bodies are structures in cells, including neurons, that have been proposed to play a role in innate immunity, by capturing VZV in cages in an attempt to prevent their replication. Therefore, we examined whether PML bodies might be involved in the prevention of productive infection in HEK 293 cells.

The normal distribution of PML bodies present was established by plating uninfected HEK 293 and ARPE cells onto coverslips and staining them with an antibody directed to PML after a 24-hour incubation period. PML bodies were present in both uninfected 293 cells (2) and uninfected ARPE cells (1), but there appeared to be more PML bodies in the ARPE cells.

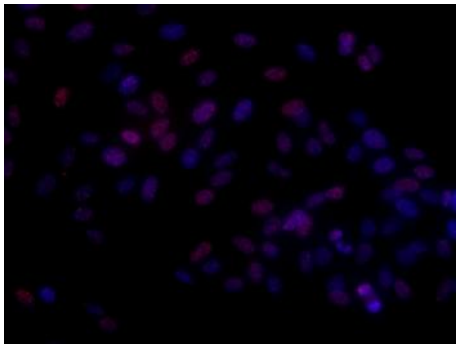

1. Uninfected ARPE cell nuclei (blue) with PML bodies (red).

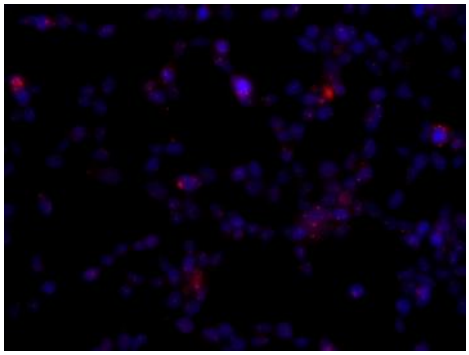

2. Uninfected HEK 293 cell nuclei (blue) with PML bodies (red). Only a few PML bodies are observed.

I then evaluated the response of PML bodies in ARPE and HEK 293 cells to VZV infection. HEK 293 cells were plated onto coverslips and incubated for 24 hours. They were subsequently infected with VZV expressing RFP as a fusion protein with ORF66 (an immediate early protein) allowing visualization of live, infected cells by RFP fluorescence. After 24 hours, the cells were fixed and immunostained with an antibody to the PML protein to visualize PML bodies and an antibody directed against another immediate early protein, ORF62, to confirm infection.

The VZV-infected HEK 293 cells displayed a very similar pattern of PML bodies to that of uninfected HEK 293 (3). By contrast, VZV infection dramatically changed the pattern of PML body pattern in infected ARPE cells: after infection, almost no PML bodies were observed (4).

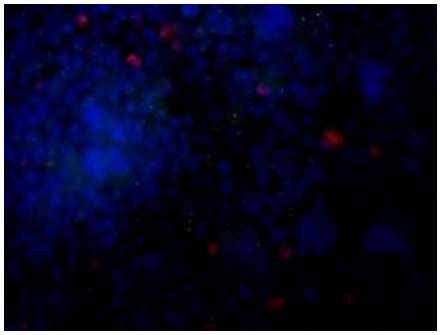

3. VZV infection does not elicit a major change in PML body distribution in HEK 293 cells. Nuclei are seen in blue, VZV66RFP infected cells are red, and PML bodies green.

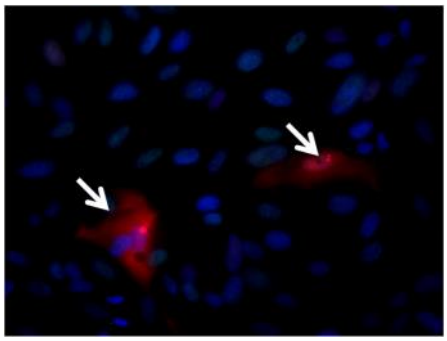

4. VZV infection results in loss of PML bodies in ARPE cells. Nuclei are seen in blue, VZV66RFP infected cells are red, and PML bodies green. Infected ARPE cell nuclei did not contain PML bodies, whereas the neighboring uninfected cells show the normal distribution of these structures.

This experiment was then repeated using a different genetically-engineered VZV. HEK 293 cells and the ARPE cells were infected with VZV that expresses GFP driven by an independent (not-VZV derived) promoter (VZV-GFP). After 24 hours incubation, the cells were fixed and stained with anti-PML. Again, PML bodies were not detected in infected ARPE cells (6) and VZV-infected 293 cells did contain PML bodies (5).

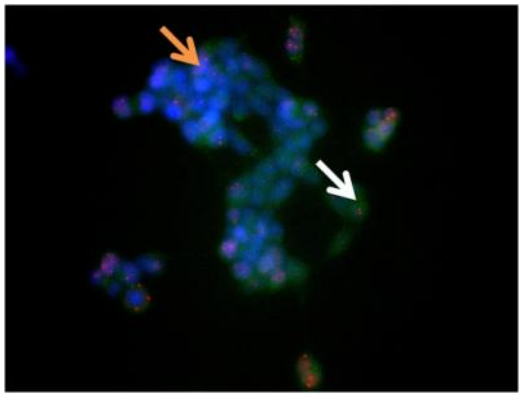

5. HEK 293 cell nuclei (blue) infected with VZV sv40 GFP (green), and showing the presence of PML bodies (red). The infected HEK 293 cell nuclei stained positive for PML bodies. The white arrow points to an infected cell, while the orange arrow points to an uninfected cell.

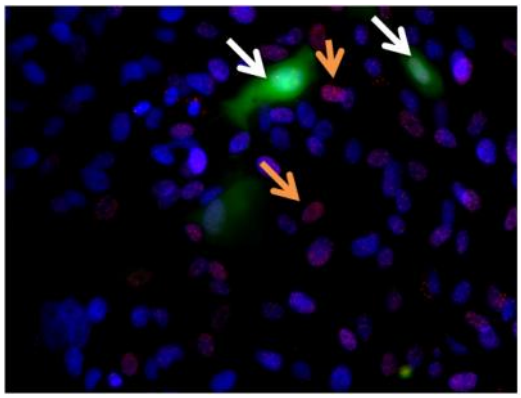

6. ARPE cell nuclei (blue) infected with VZV sv40 GFP (green), and showing the presence of PML bodies (red). Infected ARPE cell nuclei did not contain PML bodies, whereas the neighboring uninfected cells show the normal distribution of these structures. White arrows point to infected cells, while orange arrows point to uninfected cells.

The complete disruption of PML bodies in ARPE cells that were infected with VZV suggests that this intrinsic immune response is not successful in preventing replication of the VZV virus in cells in which VZV elicits a productive infection. In contrast, the presence of PML bodies in HEK 293 cells that were infected with VZV suggests that PML bodies could be involved in the inability of HEK 293 cells to undergo productive infection. Further studies are needed in order to determine the contribution of PML bodies and other innate immune responses in preventing VZV replication in 293 cells.

An additional small project I performed involved testing a newly-developed antibody. Anti-GFP antibodies can be used in order to enhance the visualization of GFP in viruses that have been engineered to express GFP, including VZV. However, the cost of these antibodies can be prohibitive. The USA national monoclonal antibody facility at the University of Iowa (DSHB) has a developed several monoclonal anti-GFP antibodies, one of which was recently acquired by the Goldstein lab. ARPE cells were infected with a GFP-expressing adenoviral vector and were immunostained with increasing dilutions of the monoclonal anti-GFP antibody (1:5, 1:10, 1:15, 1:20, and 1:25). Alexa 594 anti mouse (that fluoresces red) was used as the secondary antibody. There was good co-localization of endogenous GFP fluorescence and the antibody staining, especially at high concentrations of primary antibody. However, the data was insufficient to determine whether or not the primary antibody could stain cells with weak GFP signals. A parallel staining was also done with a commercial anti GFP rabbit antibody that produced a stronger signal than the newly developed DSHB antibody.

BIOLOGY :: WIDES LAB

Avinoam Levin (Yeshiva College) "Testing new Genes for Cooperation with Ten-m "

The teneurin gene family has been shown to mediate neuronal connection formation, axonal outgrowth, axon guidance, synaptic matching, and the maintenance of neuromuscular junctions among others. There are two teneurin genes in Drosophila: Ten-m and Ten-a. Many roles are known for these teneurins, yet little is known of their signaling pathways. Furthermore, proteins found to interact with teneurins have few pathway associations. This suggests that they participate in pathways yet to be defined.

A physical interaction in human cells between a protein involved in autophagy and a teneurin protein raised the possibility that a similar interaction occurs for that protein's homolog and Ten-m in Drosophila. However, first we had to produce this autophagy protein in Drosophila from a transgene before testing this hypothesis. Using Gateway, we recombined the autophagy gene with a Myc tag into a

vector and transformed it into bacteria. We then transfected the gene into cell culture. Through a Western Blot we found that we can in fact produce the protein. Whether or not the protein interacts with Ten-m can now be directly tested. The next step will be to ask, "is it an essential gene?" That next step would be to knockdown the gene through RNAi and knockout the gene by deleting it from the genome. This will give us greater insight into the as yet poorly defined Ten-m pathway.

Also in mammals, Ten-m has been shown to interact physically with a neuronal protein. The question we will now have is, is this interaction functional? What exactly is this interaction accomplishing?

By knocking down this protein's gene using a Gal4 driver to drive RNAi, we found phenotypic abnormalities in the TN, SN, ISN nerves, and in the CNS scaffold. This implies that this protein cooperates with Ten-m in its neuronal developmental function.

MOLECULAR BIOLOGY :: COHEN LAB

Sara Lis (Stern College) "The Role of SIRT6 in Metabolism and Beta Oxidation "

The As modern science and medicine have increased human longevity, age-related metabolic diseases, such as hypertension and diabetes type II, have risen in prevalence. For years, it has been known that a calorie-restricted diet slows aging and extends lifespan. Thus, it is possible that calorie restriction may be able to moderate the effects of metabolic diseases. Professor Haim Cohen's lab is concerned with this relationship and researches the metabolic pathways, primarily focusing on the SIRT6 enzyme. SIRT6 is part of the sirtuin family, a group of NAD+-dependent deacetylases that have been shown to be involved with the metabolic pathway and critical in the regulation of longevity.

Previously, Professor Cohen's lab has shown that SIRT6 is, in fact, involved with the metabolic pathway and regulating diets. In a past experiment, SIRT6 levels increased in response to caloric restriction, indicating that SIRT6 may be a regulator of the metabolic response to caloric restriction. In addition, mice deficient in SIRT6 were small and had metabolic deficiencies compared to normal mice, and died prematurely, displaying multiple aging-like phenotypes. Furthermore, mice that were genetically altered to overexpress SIRT6 were found to be able to maintain normal homeostasis when fed a high-calorie diet compared to their wild-type littermates, again indicating the enzyme's role as a regulator in the metabolic pathway. Male mice overexpressing SIRT6 had an extended lifespan of about 15% compared to normal mice.

Since research showed that SIRT6 is connected to metabolism and high-fat diet, we decided to investigate the role of SIRT6 in beta-oxidation, the process of breaking down fatty acids during starvation. Recent research performed in our lab included treating both normal mice and mice overexpressing SIRT6 with WY 14,643, a specific PPARA activator which activates beta-oxidation. This treatment mimics starvation possibly by activating SIRT6. We performed a genome-wide microarray analysis to measure over 30,000 genes in both normal and SIRT6 mice. We analyzed the data and found several beta-oxidation genes were indeed specifically altered in SIRT6 mice, confirming our initial hypothesis that SIRT6 regulates beta-oxidation. Further validations using real-time PCR are necessary to finalize these exciting preliminary results. To this end, specific gene sequences were analyzed and primers were ordered for these genes for qPCR.

In addition to the changes in gene expression, we wished to find a phenotype in SIRT6 mice connected to beta-oxidation. Thus, we excised livers of WY-treated mice and prepared them for analysis at Duke University. Samples are currently undergoing analysis to measure acyl-carnitine levels, a marker of beta-oxidation in tissues. This is a metabolite produced by breakdown of fatty acids that occurs during beta-oxidation. Positive results could explain the mechanism by which SIRT6 protects against high fat diet, and may partially explain the longevity enjoyed by SIRT6 mice.

In addition to WY treatment, in order to conclusively find a phenotype for beta oxidation in SIRT6 mice, another set of mice were starved in parallel to the WY treatment. These mice were placed in metabolic cages, which have been calibrated to regularly measure various physiological patterns, such as food/drink intake, activity, RER (respiratory ratio) and temperature of each mouse. After the normal and starvation period (which was performed over a number of days) the data was analyzed to find changes in mitochondrial activity. During starvation, most energy comes from beta-oxidation in the muscles as opposed to glycolysis, and therefore positively correlates with the RER ratio. The data showed that the RER levels of the SIRT6 overexpressed mice were significantly higher than the levels of the normal mice, indicating that SIRT6 may play a role in maintaining oxygen levels during caloric restriction. These preliminary results give a strong indication that SIRT6 positively regulates beta-oxidation during starvation, and possibly high fat diet as well.

These results and future results hold much promise in using SIRT6 as a potential therapy for various metabolic diseases.

MOLECULAR BIOLOGY :: NIR LAB

Ahava Muskat (Stern College) "The Effect of 'Molecule 260' on Pancreatic Cancer Cells"

In Professor Uri Nir's laboratory, the Fer kinase, a molecular trigger for cancer cell proliferation and metabolism is currently being studied. The Fer kinase sustains cancer cell survival even while the cell is under starvation conditions. Cancer cells tend to undergo mitochondrial transformations with the purpose of maintaining specific metabolic needs as well as ensuring their ability to promote tumor growth. The Fer kinase functions in this way. Some specific functions of the Fer kinase include regulation of cytoskeletal organization, cell adhesion, cellular response to cellular insults, and the ability to protect cells from ionic radiation. When tested, Fer was found in all human malignant cell lines. Moreover, Fer was expressed in higher levels in malignant tumor cell lines than in benign tumor cell lines. Additionally, when Fer was down regulated in breast, prostate and colon carcinoma, proliferation of these cells was impaired. Down regulation of Fer was also found to prevent breast and lung tumor formations.

These studies and others prompted Nir's lab to study the intracellular tyrosine kinase in depth. Additionally, the laboratory studied the truncated version of Fer called FerT. FerT has a slightly different molecular structure than Fer. While the two enzymes maintain the same kinase domains, the N-terminal tails differ and FerT lacks the N-terminal functional elements found in Fer. In Professor Nir's laboratory, both of these enzymes were shown to be associated with mitochondrial complex I in colon carcinoma cells. Fer functions with regard to complex I to maintain steady metabolism of cells even under low nutrient and oxygen environments. Moreover, when Nir's lab etopically transfected non malignant cells with Fer directed towards the mitochondria (they used NIH3T3 mouse embryonic fibroblast cells), the cells were transformed to having the ability to form tumors. Seeing the immense and significant capabilities endowed to cells when up-regulated with Fer, Nir's laboratory is currently in the process of creating a drug to target this kinase with the hopes that if major metabolic capabilities of cancer cells could be impaired, cancer cells would die.

After an extensive series of cellular experiments, Nir's laboratory discovered that a specific molecule-"molecule 260"- when applied to certain carcinoma cells, was successful in targeting the intracellular tyrosine kinase Fer; specifically when this molecule was applied to prostate, colon and breast cancer cells. Currently, we are in the process of researching the effect of "molecule 260" on pancreatic cancer cells as well. One experimental technique that is being used to determine the effect of "molecule 260" on pancreatic cancer cells is through analyzing the results of several MultiTox-Fluor Multiplex Cytotoxicity Assays. This assay involves two different types of proteases that work respectively on dead and live cells determining the cells viability or cytoxicity (death) after incubation with a specific substrate. The data is normalized and, thus, it is able to be easily analyzed. We performed this assay a number of times and recorded the results of Panc1 cells (pancreatic cancer cells) applied with "molecule 260" in different concentrations and exposure durations for 24, 48, and 72 hours. The results indicated that the number of live cells decreased as the concentration of "molecule 260" increased. Additionally, the number of live cells decreased from Panc1 cells applied with concentrations of "molecule 260" incubated from 24 hours to 72 hours, with the Panc1 cells incubated with "molecule 260" for 72 hours maintaining the least number of live cells after performing the assay. The results of this assay maintained in fact "molecule 260" does target the key enzyme Fer and impairs its ability causing metabolic functions of cancer cells to be compromised. Additionally, the targeting of Fer possibly impaired the cells' cytoskeletal organization and cell adhesion. All of these functions are vital to a cells' viability. As Fer was targeted and these functions were impaired, the cells died indicating a lower number of live cells.

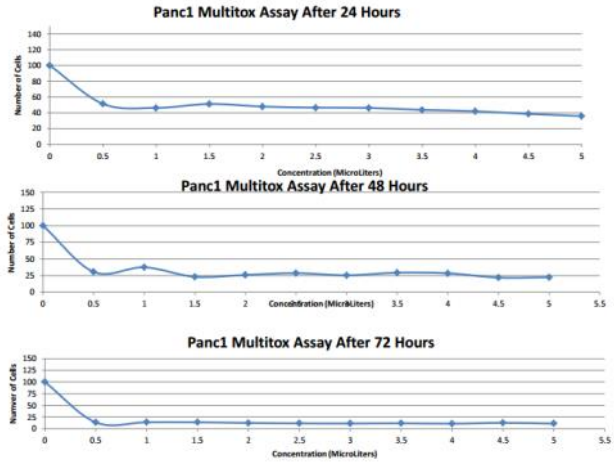

We then continued with an analysis of a series of Western Blots. The protein extractions used as samples for the Western Blots were extracted from 24hr, 48hr, and 72hr incubations of pancreatic cancer cells with "molecule 260" and their respective incubations with a control molecule. The results of the Western Blots were meant to indicate if the death of these cells is mediated by autophagy. In all cells, LC3, a soluble microtubule-associated protein aids in the process of autophagy. When autophagy is induced, LC3, or LC3-1, forms LC3-II through its conjugation with phosphatidylethanolamine. One of the known purposes of LC3-II's formation is to facilitate the fusion of autophagosomal membranes with lysosomes for degradation. Analyzing the relative width of the LC3-1 and LC3-2 bands indicate the levels of autophagy induced.

The secondary antibodies used in the Western Blots were mouse antibodies.

The results of the Western Blot testing pancreatic cancer cells incubated with "molecule 260" indicated that the pancreatic cancer cells applied with "molecule 260" showed thicker LC3-II bands than pancreatic cancer cells applied with a control molecule demonstrating that pancreatic cancer cells applied with "molecule 260" activated autophagy, probably in order to survive. Cancer cells applied with the control molecule did not show clear autophagy induction.

Currently, the laboratory is processing the results of the other Western Blots to determine if the pattern continues with pancreatic cancer cells incubated with "molecule 260" for 48 hours and 72 hours. The laboratory will continue analyzing the effect of "molecule 260" on pancreatic cancer cells through other methods such as immunohistochemistry. Eventually, the goal of Professor Nir's laboratory is to develop a drug using "molecule 260" to kill different types of carcinoma cells by targeting Fer.

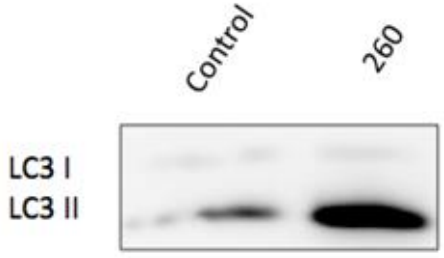

Results of Western Blot of extracted proteins from pancreatic cancer cells applied with a control molecule and "molecule 260" and incubated for 24 hours.

MOLECULAR BIOLOGY :: MOTRO LAB

Michal Schechter (Stern College) "Creation of double mutant cells for Nek3 and Nek5 kinases by CRISPR/Cas9 method and the localization of Nek5 in the lung "

Transition from one cell cycle phase to another occurs in an orderly fashion and is regulated by multiple evolutionary conserved proteins. In our lab, we researched the Nek kinase family, which is known to be involved in the transitions between the cell cycle phases. The mammalian NIMA-related kinases (NRK's) genes, which are designated as Nek1-11, encode for evolutionarily conserved serine/threonine kinases, structurally related to the fungal mitotic regulator, NIMA. As implied by its name (Never In Mitosis A), the catalytic activity of *Aspergillus nidulans* NIMA is indispensable for mitotic entrance. In conditional absence of NIMA activity, fungal cells arrest in G2, exhibiting interphase microtubules and uncondensed chromosomes. Overexpression of NIMA induces a mitosis-like phenotype, including premature chromatin condensation and abnormal mitotic spindles.

Several mammalian Nek kinases (including Nek2, 6, 7, and 9) have shown to be critical for the cell cycle and the centrosome cycle. However, the functions of the other mammalian Nek kinases are less obvious. The catalytic domains of Nek1, Nek3, Nek5 and are highly homologous. Therefore, they are sub-grouped into the same NIMA-related kinase sub- family. Nek1 has shown to be critical for primary cilium genesis, and mutants for Nek1 exhibit dwarfism, sterility and polycystic kidney disease. Nek3 is expressed in the brain, and is involved in microtubule dynamics. Very little is known about Nek5, so our lab created knockout mice to Nek5. There was no apparent phenotype for these mice, they were healthy and fertile, and did not exhibit developmental problems.

Due to the possibility that Nek3 compensates for the absence of Nek5 in the mutant mice, the first goal of my project was to create a double mutant for Nek3 and Nek5 in cells. We attempted to create this double mutant by using the CRISPR/Cas9 system. CRISPR is a new method which is based on the Cas9 system in bacteria. The CRISPR/Cas9 system is usually used for targeted gene mutation or editing. We planned and constructed unique genomic sequences for Nek3 and Nek5 (designated single guide RNA-sgRNA), which possessed recognition sites for endonuclease Cas9. When the Cas9 protein recognizes the sgRNA, the genomic Nek3 and Nek5 loci are cut out and the double mutation is thereby created. Based on the phenotype of Nek1, we expect to see an abnormal phenotype in the cell cycle or in the DNA damage response of the double mutants for Nek3 and Nek5.

Since the mutant mice for Nek5 do not have an obvious abnormal phenotype, our lab also checked to see in which specific organs Nek5 is expressed. Based on previous Northern blotting analysis, we concluded that Nek5 is mainly concentrated in the brain and lung. In order to identify the exact areas expressing Nek5, we took advantage of the lacZ which the lab had inserted into Nek5 locus in the knockout mice. The lacZ was inserted downstream of the endogenous Nek5 promoter, thus lacZ staining is expected in areas where Nek5 is expressed. We were able to demonstrate that lacZ staining (and thereby Nek5) is specific to the ----arterioles in the lung, while no expression could be seen in the alveoli or other structures in the lung. As the arterioles are ciliated, it may be speculated that Nek5 is involved in cilia genesis (as has been shown for Nek1).

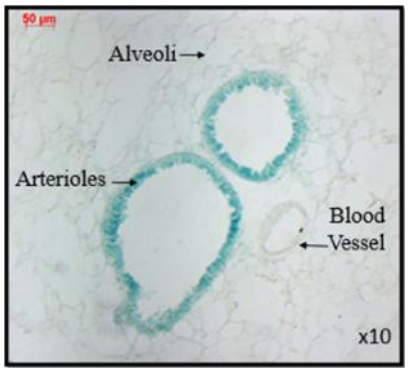

Figure 1. Beta-galactosidase staining of a lung tissue from a heterozygote Nek5 mouse (x10).

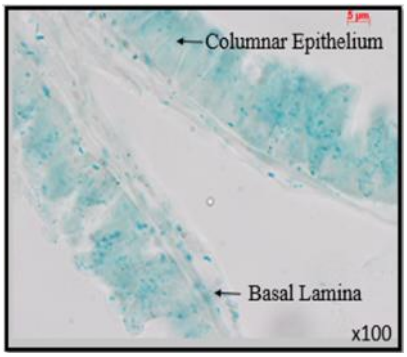

Figure 2. Beta-galactosidase staining of a lung tissue from a heterozygote Nek5 mouse (x100).

MICROFLUIDICS :: GERBER LAB

Alexander Straus (Yeshiva College) "Microbeads as an Alternative to Surface Chemistry for High Throughput Analysis in Microfluidic Devices "

Microfluidic chips are incredibly powerful devices in which thousands of experiments such as immunological or enzymatic assays can occur in parallel. This enables high throughput analysis of protein-protein, or DNA-protein interactions. A microfluidic chip consists of two layers of PDMS polymer on top of a glass slide. The top layer of PDMS (known as the "control" layer) is composed of a network of microchannels that swell when filled with water and act as a valve system for the underlying layer. The bottom layer (known as the "flow" layer) contains numerous interconnected unit cells which are each in turn composed of two chambers, the DNA and Interaction chambers. The connection between individual unit cells is controlled by "sandwich" valves while fluid flow between DNA and Interaction chambers is moderated by the "neck" valves (see Figure 1. and Figure 2.).

For example, DNA marked with a florescent tag is printed by a machine onto a microarray which is then aligned inside the DNA chambers. The neck valve is shut, and the protein of interest is flowed through the chip and captured in the Interaction chambers by "button" valves. Afterwards, the protein of interest attaches to a tower-like protein complex and is immobilized on the glass slide. This large protein-complex is referred to as surface chemistry. The formation of appropriate surface chemistry on a glass slide is a multi -step process that can take up to 2-2.5 hours.

Next, the excess protein is washed away and the sandwich valves are shut, isolating the unit cells, while the neck valves are opened. The contents of the DNA chambers diffuse into the Interaction chambers and come into contact with the protein of interest. Positive interactions occur when the DNA or its product bind with the protein of interest and are subsequently also immobilized on the glass surface. Finally, the sandwich valves are opened and the unbound DNA or its products are washed away. The microfluidic chip is placed into a fluorescent scanner to detect any positive interactions.

The rate determining step in the process described above is the time required for the creation of appropriate surface chemistry on the glass slide. The goal of our research is to greatly reduce experiment run-time by replacing standard surface chemistry with microbeads as a binding substrate for the protein of interest. Thus far, with minor modifications to manufacturer instructions, we have successfully bound Biotinylated IgG to Streptavidin microbeads. IgG acts as a bridge and binds the protein to the bead. Protein-free IgG, however, tends to bind to proteins already bound to other beads and cause aggregation; we reduced aggregation by saturating any unbound IgG with Biotin-BSA.

We are simultaneously working with several different microbead brands (Chemicell, Pierce, and Dynabead), bead sizes (0.2, 1 and 2.8 micron) and concentrations in order to optimize bead flow and capture, and to further reduce aggregation within the device. Our last step will be to perform a standard microfluidic assay utilizing surface chemistry, and then reproduce the results with microbeads. Our hope is that microbeads will replace conventional surface chemistry in microfluidic experiments. Microbeads with the appropriate protein attached could easily be prepared in batches ahead of time and loaded into the chip when needed (See Figure. 3). Eliminating surface chemistry in microfluidic systems will allow for even more rapid discovery of new biochemical pathways and interactions.

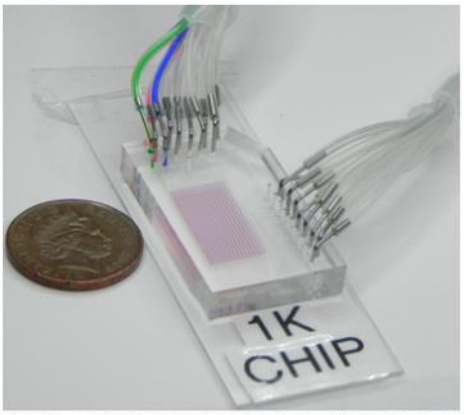

Figure. 1 A PDMS microfluidic chip with 1000 unit cells

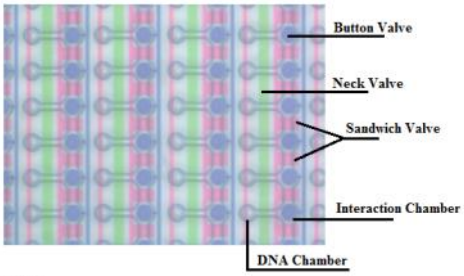

Figure. 2
Microchannels and valve system magnified. The chip was filled with colored dye to help distinguish the different components of the channel and valve systems.

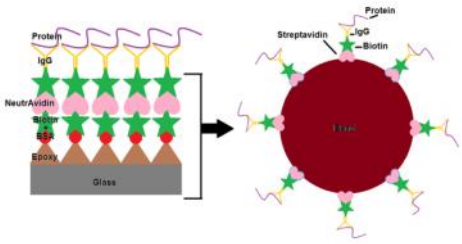

Figure 3. An illustration of basic surface chemistry compared to a microbead.

MICROBIOLOGY AND BIOENGINEERING :: BANIN LAB

Adina Wakschlag (Stern College) "The Production of biethanol from the green algal species, *Ulva lactuca*: The role of ulvan-degrading enzymes in a synthetic operon"

Ulva lactuca is a species of green seaweed favorable from many standpoints for the production of ethanol fuel via the conversion of its polysaccharides—namely, ulvan, comprised of rhamnose, glucuronic acid, xylose, and glucose*—into ethanol. In an attempt to bioengineer a microorganism that will carry out this entire conversion process, five genes coding for ulvan-degrading enzymes of native ulvan-degrading bacteria were isolated, genetically sequenced, and quantitatively characterized as collectively efficient in ulvan sacchrification. In this research effort, the first of several ulvan-degrading enzymes** was constructed into what will be a synthetic operon that will facilitate the sacchrification of ulvan. The subsequent ulvan monomers are to be fermented into ethanol through modified metabolic pathways of the same organism, *Escherichia coli* KO11.

In order to carry out the most efficient sacchrification of ulvan, we employed a synthetic operon system developed by the laboratory of Ron Milo at the Weizmann Institute of Science (Rehovot, Israel). This project aims to create a library of synthetic operon permutations, consisting of six different ribosome binding sites (RBSs A-F) and five separate genes for specific ulvan-degrading enzymes necessary for complete ulvan degradation. The purpose of the utilization of varied RBSs is to fine-tune the synthetic operon by pinpointing the appropriate expression levels of each enzyme. Each RBS demonstrates unique affinity to the ribosome, corresponding to the distinct level of the subsequent gene's expression. (See Figure 1a for a qualitative depiction of RBS-dependent protein expression levels.) At the end of the synthesis process, the operon with the combination of RBSs that yields the most effective ulvan-degradation will be selected.

During the initial assembly of the synthetic operon, the resistance cassette for the antibiotic, chloramphenicol (Cm^R), is sewn onto the genetic inserts and ligated to temporary host plasmids pNIV A-F (each pNIV accommodating a unique RBS) in order to allow for selection of plasmids containing the gene of interest. pNIV plasmids and genes with Cm^R are restricted and ligated to one another, one gene at a time (utilizing only one Cm^R), until all five genes are incorpor45ated into a single insert. The end result is a library of 6^5 combinations of the complete operon. Figure 1b below broadly outlines the steps of this goal using Genes 1 and 2 and their resulting library as a model for all the genes. The synthetic operon in its numerous forms is then transferred out of the pNIV plasmids and into pTAC, a plasmid that facilitates better gene expression than pNIV. Subsequent biochemical assays will determine the most efficient ulvan-degrading operon permutation, and the plasmid containing that sequence will be transformed into the final organism, *E. Coli* KO11. Presently, the research effort at hand has successfully integrated Gene 1 of the operon into pNIV A-F plasmids, setting the stage for further synthesis of the operon.

*Ulvan's sugar sequence is presented (in Percival & McDowell, 1967) as follows: GlcA(1→4)Rha sulfate(1→4)GlcA(1→3)Xyl(1→4)

Rha sulfate(1→3)Glc(1→4)Xyl

**Names of genes, enzymes, and native ulvan-degrading bacterial strains cannot be disclosed at this time due to patent issues. Genes are referred to using arbitrary labels ("Genes 1-5").

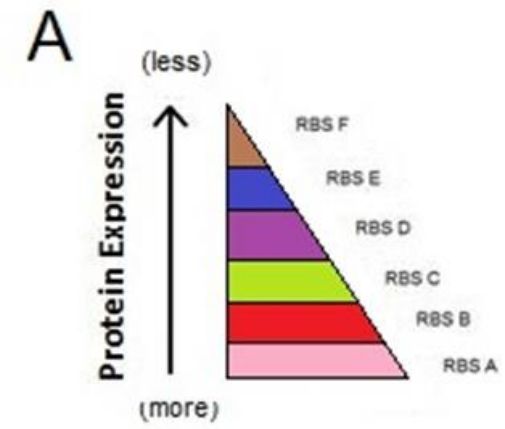

Figure 1a. Levels of protein overexpression decrease from RBS A to F.

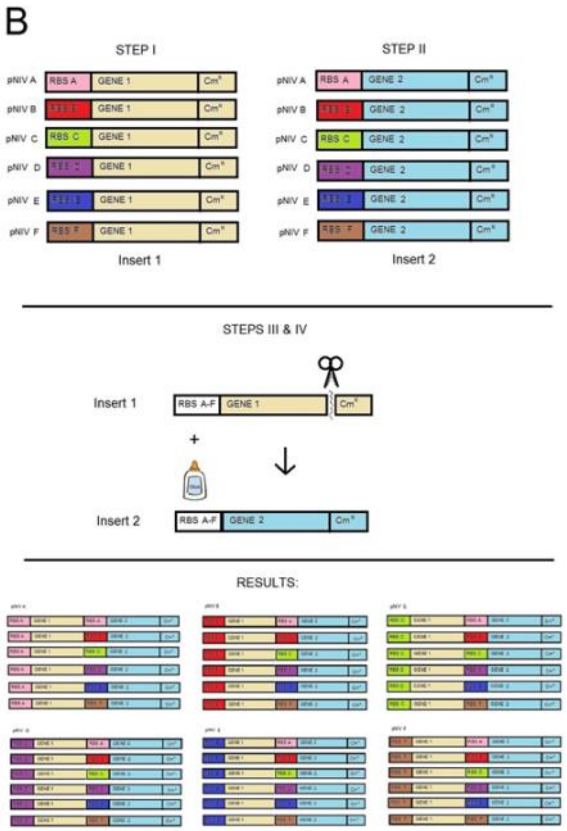

Figure 1b. General outline of operon synthesis with Genes 1 and 2, the first steps in creating the operon library.
Step I – Ligate Gene 1 + Cm^R (Insert 1) to pNIV A-F plasmids;
Step II – Ligate Gene 2 + Cm^R (Insert 2) to pNIV A-F plasmids;
Steps III and IV - Remove Cm^R from Insert 1 via restriction and ligate Insert 2 to newly modified Insert 1;
Steps III and IV result in the above (6^2) combinations of operons in temporary pNIV plasmids.

COMPUTATIONAL IMMUNOLOGY :: MEHR LAB

Tamar Wasserman (Stern College) "Mathematical Modeling of Natural Killer Cells in the Liver "

There are four stages of development in Natural Killer Cells, and these stages are defined by whether or not the cell has one, both, or neither of two receptors on its membrane: $CD27^-Mac\text{-}1^-$ —> $CD27^+Mac\text{-}1^-$ —> $CD27^+Mac\text{-}1^+$ —> $CD27^-Mac\text{-}1^+$. These two receptors are specifically for NK cells in mice; humans have different receptors, including CD56, which can also have different levels of expression ($CD56^{bright}$ and $CD56^{dim}$).

The goal of the experiment was to analyze the dynamics of development of NK cells in the liver of mice. Eventually, this should lead to conclusions being drawn about NK cells in humans. By using a mathematical model, we found the rate at which the NK cells at each of the four stages enter the liver, proliferate, transition to the next developmental stage, exit the liver, or die. We also found the carrying capacity for each population in the liver.

The data for the mathematical modeling was received from Eric Vivier's lab in France. The lab depleted NK cells in a number of mice, and harvested NK liver cells from a few mice every few days. The total number of cells and the fraction of BrdU labeled cells (to track proliferation rates) were measured for each mouse. These measurements were used for the modeling.

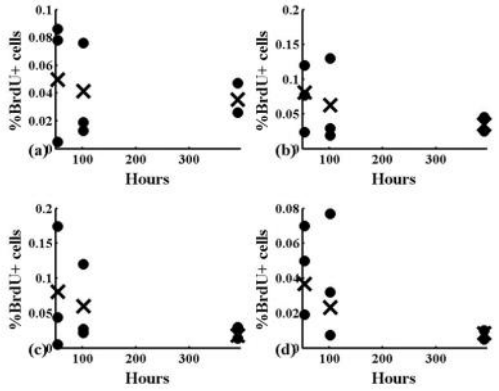

Figure 1. Fraction of labeled cells for all four populations. Dots represent experimental data (one dot per mouse), X's represent results from best-fit simulation.

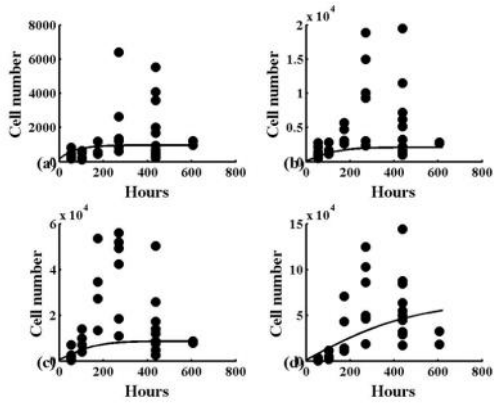

Figure 2. Total cell numbers. Dots represent experimental data, lines represent results from best-fit simulation.

From the results of the mathematical modeling, we were able to conclude that NK cells at the later stages of development have longer residence times. Cells in Stage 4 have much longer residence times than the cells in the earlier stages because the cells in Stage 4 are mature and in their fully-functioning state. Therefore, they remain in the liver in this stage for longer, in order to function as fully -developed NK cells.

We also found that Stages 3 and 4 have the highest carrying capacities because these are the cells that are most needed in the liver, which is a more mature lymphoid organ (in comparison to the bone marrow). The liver therefore "reserves" more space for these mature cells.

Lastly, we found that Stage 4 has the highest rate of influx of NK cells from outside the liver. Most cells enter the liver at this mature stage (as opposed to at earlier stages of development) because the liver is a mature organ and requires these cells for functioning. It is likely that it is more efficient for the cells to mature in the bone marrow and then migrate to the liver, instead of entering the liver at Stage 1 and maturing in the liver. (In total, it takes an NK cell approximately 155 days to advance through the first 3 stages in the bone marrow, whereas it takes 348 days in the liver.)

NEUROSCIENCE / PSYCHOLOGY

Left to Right: A. Huttel, T. Annenberg, L. Weiss, S. Schneider, D. Watman, S. Robinson, B. Weisinger, T. Kamdjou, T. Golubtchik, N. Wakschlag

PSYCHOLOGY :: GILBOA-SCHECHTMAN LAB

Naomi Wakschlag (Stern College) and Tamar Annenberg (Stern College) "Pictorial-IAT as a Measurement of Implicit Social Anxiety"

The self is a multifaceted structure that functions in the two separate modes of implicit and explicit self. Implicit self-associations can be measured with the Implicit Association Task (IAT) (Greenwald & Farnham, 2000). The IAT is often used to assess implicit self-esteem, an evaluation of the self, and in this way can be used as a tool to indicate social anxiety. Trower and Gilbert (1989) theorized that individuals with social anxiety interpret social interactions as determinants of status in a dominance-submission social hierarchy viewing themselves as submissive and others as dominant.

The current study examines self-esteem as it relates to Trower and Gilbert's (1989) theory of social anxiety. We used a single-category self-esteem IAT to compare associations of the attributes of self and not-self with the attribute of dominance. Slabbinck, De Houwer, and Van Kenhove (2011) demonstrated that since the source of implicit associations is pre-verbal experience, a pictorial-IAT can be used as a valid measure of such associations. Accordingly, in the current study we presented our dominant stimuli in the form of pictures of dominant individuals, whereas thus far self-esteem IATs have presented stimuli only in the form of words.

The first aim of our study was to determine whether a self-esteem IAT with some stimuli presented as pictures would yield results similar to those of non-pictorial measures of implicit self-esteem. Previous studies measuring implicit self-esteem have established that most individuals, in any sample, positively associate concepts relating to the self (Greenwald & Banaji, 1995). Therefore, we set out to determine whether our pictorial dominance self-IAT would result in similar self-associations. In addition, past studies have examined the correlation between explicit and implicit self-esteem. In contrast to implicit measures, explicit measures are often influenced by the individual's perception of self. Positive correlations between explicit and implicit self-esteem have been found, but have been weak, possibly as a result of the influences on responses to explicit self-report measures (Greenwald & Farnham, 2000). The second aim of the current study was to look for correlations between explicit and implicit self-esteem, and to compare our findings to the results of previous studies.

In our study, we measured explicit and implicit self-esteem in eleven undergraduate students. We used the Rosenberg Self-Esteem Scale to measure explicit self-esteem, and a pictorial-IAT to measure implicit self-esteem. In the IAT, the participants were presented with stimuli which were related to the attributes of self, not-self, or dominant. The participant was asked to sort each stimulus into the appropriate attribute by pressing specified keys on a keyboard. If a participant strongly associated himself with dominance, he would be faster at sorting the self and dominant stimuli together. If a participant strongly associated others with dominance, he would be faster at sorting the not-self and dominant stimuli together. This comparatively stronger association between others and dominance would indicate a lower level of implicit self-esteem.

Analysis of the data revealed that, except for one low explicit self-esteem score, all explicit self-esteem scores fell within the normal

range, and that six of the participants had positive implicit self-esteem scores. No overall correlations were found between explicit and implicit self-esteem. These results show that our pictorial-IAT was not fully consistent with the results of previous studies. Based on the previous studies on implicit self-esteem, we expected to find all positive implicit self-esteem scores. While six of the scores were positive, indicating some consistency with previous studies, five of the scores were negative. This is particularly surprising since all but one of our participants reported normal explicit self-esteem. Because our results indicated that our pictorial-IAT was not fully consistent with other measures of implicit self-esteem, we could not arrive at any conclusions regarding the correlation between explicit and implicit self-esteem.

Limitations of the current study include small sample size and use of only one explicit self-esteem measure. Future research could explore the validity of a pictorial-IAT, using a larger sample size and multiple measures of explicit self-esteem. Future research could also compare results of a pictorial-IAT with results of a validated word-IAT.

NEUROSCIENCE :: OKUN LAB

Tamar Golubtchik (Stern College) "Assessing pattern completion in spatial navigation"

Spatial learning is the process by which animals encode information about the environment in order to facilitate navigation through space and recall locations of motivationally relevant stimuli. Pattern completion refers to the ability to recall a previously learned location in space based on degraded or missing visual cues. Computational models of the hippocampus, a brain region linked with learning and memory, suggest that the CA3 subregion of the hippocampus can perform pattern completion. The Morris Water Maze (MWM) is a common behavioral task that assesses hippocampus-dependent spatial learning in rodents. In this task, mice are given three consecutive 90 second trials to find a hidden platform within a circular water pool. Once on the platform, mice are given 30 seconds to rest and observe the visual cues in the room (Figure 1). If the mouse is unable to find the platform, it is gently guided there. Latency to reach the platform and path efficiency are measured to determine performance of the mice in this task. We have utilized the MWM in order to test spatial pattern completion in healthy mice. To accomplish this, 45 young male mice were maintained in a controlled 12:12 hour light-dark reversed cycle. The mice were kept in a completely dark room, lit only with an infrared (IR) light to enable video tracking using an IR-sensitive camera. Four computer screens were placed on each wall in the room provided visual cues for the mice.

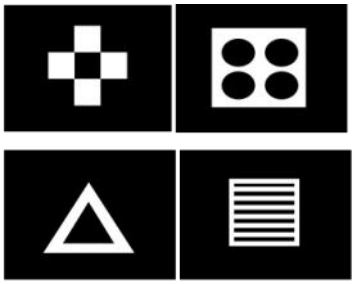

Figure 1: Four illuminated cues used during hidden and probe stages with 12cm x 12cm platform in upper right quadrant. Four LCD screens, each with one illuminated shape, were placed on each wall around the pool in plain sight of the mouse at a height of 118cm above the ground.

Initially, a visible platform stage was performed to assess the motivation of the mice as well as any visual or motor impairment that could potentially disqualify mice form this experiment. Following training of the mice using the hidden platform, during which optimal latency to reach the platform was obtained (Figure 2), mice were tested in the probe stage. During the probe stage, the platform was removed and the mice were divided into five groups, each with nine mice. Each group was tested and exposed to 4, 3, 2, 1 or 0 cues respectively. It was hypothesized that the groups of mice given more cues (4 or 3) would spend more time in the quadrant of the pool that had contained the platform compared with mice exposed to fewer visual cues.

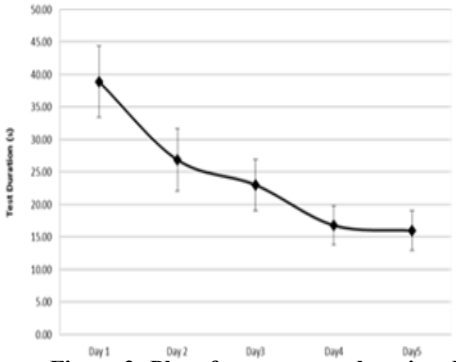

Figure 2: Plot of average test duration during the hidden platform stage with a 12cm x 12cm platform.

During the probe test, as hypothesized, the mice spent the most time in the platform quadrant with either four or three available cues (figure 3, 4a, b). When there were only 2, 1 or no cues available, the mice no longer spent a large amount of time in the platform quadrant (Figure 3, 4c, d, e).

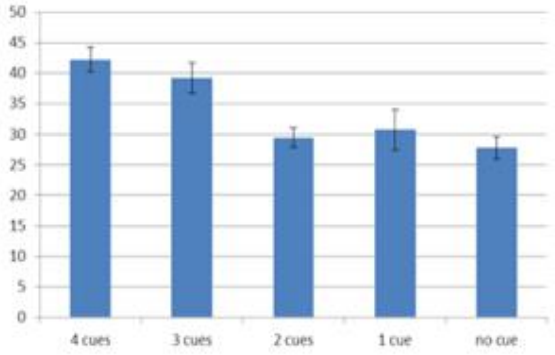

Figure 3: Graph of average time spent in lower right quadrant during probe test, based on how many visual cues were illuminated.

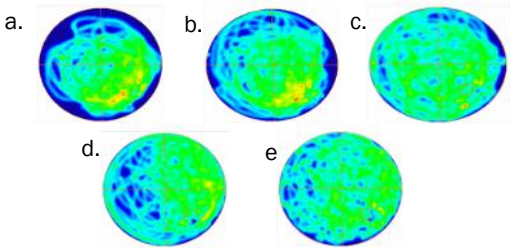

Figure 4: Occupancy plots illustrating the amount of time, on average, that the mice spent in each quadrant of the pool during the probe stage. This data is based on the number of visual cues present: (a) 4 cues, (b) 3

As can be seen in figure 4, the mice spent the majority of swimming time in the platform quadrant (lower right quadrant) when presented with either 4 or 3 visual cues. When presented with 2, 1 or no cues, the mice spent relatively equal amounts of time in each of the quadrants. These findings are consistent with our assumption and suggest the mice use the mechanism of pattern completion during the MWM task.

BRAIN STEM AND EXECUTIVE CONTROL :: GEVA LAB

Adam Huttel (Queens College) "Neonatal Brainstem Effect on Executive Control at 8 Years"

The vertical integrative model demonstrates that brainstem integrity at preterm birth (33-38 weeks gestation age) affects later maturation of higher level brain development. The brainstem is directly responsible for homeostatic processes such as sleep and breathing. However, evidence shows that deficits in early developing brainstem influence later processes such as limbic controlled changes in attentional and emotional state. It is also thought that such early dysfunction will influence higher order processing, such as executive functioning in the prefrontal cortex, which is known to mature in late childhood (responsible for planning, problem solving, and decision making).

The current project aimed to further advance knowledge regarding how brainstem dysfunction influences executive control. We hypothesized that neonatal brainstem dysfunction will influence the maturation of other brain regions later in life, including the prefrontal cortex (i.e., executive control).

In order to test this, a prospective longitudinal study was conducted from birth through 10 years of age. Auditory brainstem evoked responses (ABR) were tested in the neonatal intensive care unit between 33-38 weeks gestation age. Groups were divided based on ABR integrity into normal and compromised brainstem functioning groups (NBSF and CBSF, respectively). When these children were 8 to 10 years of age they underwent the Attention Network Task-Children (ANT-C) in the lab using gaze tracking technology to measure durations of fixations throughout the task. The ANT-C tests the functioning of 3 attention networks (alert, orient, and executive control) by presenting three fish in a flanker task, in which the child was instructed to detect the direction that the middle fish faced by pressing the corresponding mouse buttons. In addition to gaze data, reaction time and accuracy were recorded.

ANCOVA analysis showed a fixation duration in the executive network main effect for accuracy ($F=7.404$, $P<.05$, $eta2 =.163$), but not for reaction time in the executive network. Gestation age was held as a covariate in these analyses. Repeated measures analyses comparing fixation durations between NBSF and CBSF groups were run for all three attention networks. Results showed no effects for alert and orient networks, and a significant network by ABR interaction effect for the executive network ($F= 6.967$, $p<.05.eta2 =.148$).

Findings suggest that 8-10 year old children's fixation durations are related to accuracy and not to response time in the ANT. Furthermore, it was found that children with CBSF showed differential patterns of gaze durations toward the executive network as compared with children with NSBF. These results indicate neonatal CBSF impacts executive network functioning at 8 years of age.

COGNITIVE NEUROSCIENCE :: BAR LAB

Talia Kamdjou (University of California, Los Angeles) "The Proactive Brain: A study of predictions through statistical learning"

Recent literature in the growing field of cognitive neuroscience has proposed that the human brain is a proactive organ that anticipates reality by constantly making predictions for the near and relevant future. One explanation for this process is supported by physiological and neuroimaging evidence and is based on analogical links. When given an input, the brain forms analogies from previously stored, elementary information and memory. In complex situations, such as social interactions, the brain combines multiple analogies from a pre-existing script of memories relevant to the situation in context in order to make the predictions. The memories may be real or previously imagined. Whereas previous research has elaborated on the process of bottom-up signals, "recognition-by-analogy" relies on top-down influences, in which the proactive mind continues to perceive the world based on an individual's previous experiences.

The Bar lab is interested in dissecting the detailed mechanism in which visual stimuli are processed and ultimately lead to associations and predictions in the brain. This project harnesses statistical learning as a tool to study top-down influences in order to manipulate and study the brain's ability to form analogies and subsequent predictions. Statistical learning postulates that humans have the ability to implicitly learn subtle statistical relationships and discrepancies from the environment. A serial reaction time (SRT) task in which subjects need to respond as fast as they can to a series of stimuli was used to assess learning.

After having gone through meticulous reading and compiling information on similar experiments, a unique and interactive experiment was designed using computer-programming software, MATLAB, with the psychtoolbox library. In one version of the SRT task, subjects were presented with a stream of individually shown characters, and were asked to indicate by a key-press if they saw a digit or letter. In another version, contour objects replaced the characters. Unknown to the subjects, the stream contained a recurring regularity of four pairs from the stimuli, repeated randomly and equally, amongst other neutral stimuli presented as distractors (sample stream shown in Fig. 1). The first stimuli of the pair was termed as the "predictor" and the stimuli following it as the "predicted." Each stimulus was shown for 200ms, with inter-stimulus intervals (ISI) of 1s, 1.4s, and 1.8s (shown with the probabilities of 50%, 30%, and 20% of the time, respectively). The experiment was followed by a familiarity post-test, and a debriefing session to assess whether or not the subject became aware of the pattern.

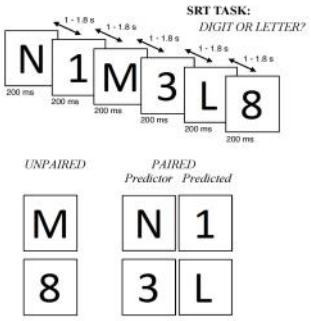

Figure 1 .

The probability associated with the stimuli cues guides for an increase in the SRTs of the "predicted," as the response times become increasingly faster when the probabilities are learned. To indicate an increase in SRTs, a 15-millisecond effect between that of the neutral stimuli and the second stimuli of the pair must be detected. Two experiments were created to accommodate the unique stimuli in order to determine which provides the greater desired effect.

A next step of the project is to examine subjects under the MEG - a functional neuroimaging technique that maps brain activity. Literature claims that the brain processes letters and digits through differing pathways and areas of the brain. The Visual Number Formation Area (VNFA) is processed through the inferior and middle frontal gyri, the fusiform gyrus, and the ventral section of the left angular gyrus. The Visual Word Formation Area (VWFA) is mainly located in the mid-portion of the left fusiform gyrus, left occipital temporal area, and the anterior cingulate gyrus. Furthermore, object contours were used as stimuli because when manipulated to form analogies and make predictions, they have been shown, among other stimuli, to activate the retrosplenial complex, parahippocampal cortex, and ventral-medial prefrontal cortex of the brain's left hemisphere.

Approximately 20 subjects have been run thus far, all of who were right-handed and ranging from 18-35 years of age. Computer programs were written to analyze the results, and although significant results have yet to be found, and more subjects need to be tested, there has been a trend – for both versions of the experiment. When aggregating the mean RT of subjects who were presented digits and letters as stimuli, a RT difference of ~10ms was found between the neutral and predicted but the outlying standard deviation lines prevent the data from being significant (Fig. 2). For the mean RT of subjects who were shown object contours a RT difference of ~15ms was found and the standard deviation lines conclude more significant results (Fig. 3).

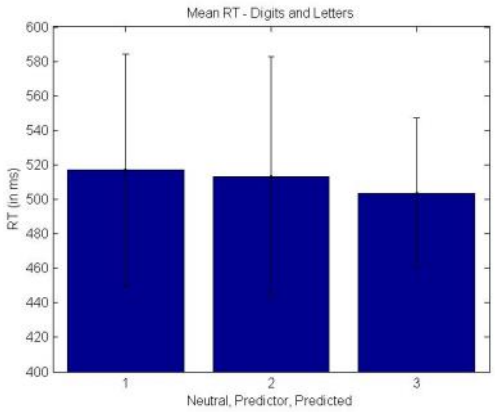

Figure 2 .

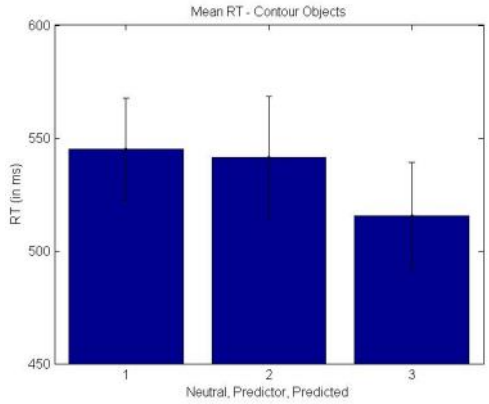

Figure 3 .

HUMAN MEMORY AND RECOGNITION :: VAKIL LAB

Sarah Robinson (Stern College) "Studies in Context Effect"

Memories are a mechanism whose purpose is to perceive information, store it, and re-use it as necessary, whether consciously or not, so one can cognitively process information which is no longer available to the sensory system. Prior research has presented numerous models describing various types of memory. Within the field of recognition memory, one such type is Context Memory – memory for the information peripheral to the target of interest. Research in context memory explores "Context Effect," the enhanced memory store for targets presented in the identical background from the initial viewing stage. For example, I organized materials for two experiments; in one, the face was the target and a scene served as context (fig.1), and in a second, the face was the target while the hat was the context (fig.2).

Though it is well documented, CE in recognition memory is somewhat of an evanescent phenomenon thereby motivating tremendous research in the subject. This ultimately led to Professor Vakil's lab becoming a leading expert in examining how target and context bind, which conditions motivate the arousal of a CE, and the individual nature of a Target and Context. Additionally, this led to Professor Vakil's proposal for a multifactorial model for the creation, maintenance, and retrieval of context memories.

The lab also aims to study the cognitive relationship between context memory and eye movements by using an SMI Eye Tracker to records participant's saccadic eye movements. This tool is used in a wide array of contexts; some use it for medical research or diagnostics, while others use it for market research. This lab uses it to test the presence of implicit learning of a sequence, to measure for the participant's focus (or lack thereof), and to measure the sequence of focused areas.

For example, I was involved in running statistical analyses on an experiment where elderly and young participants visually followed and hit a correlated keyboard key upon seeing a black dot as it sporadically appeared in 4 zones on a computer screen. Unbeknownst to the participants, there was a cyclical sequence governing the transition between the cues, thus making the responses predictable. In analyzing the motor response (from hitting the keyboard key) and the saccadic movements (recorded in the Eye Tracker), results indicated that elderly patients had significantly longer motor responses yet had identical saccadic responses to the stimuli. This indicated that elderly participants, like the young participants, were able to learn the implicit sequence of dots, even if their motor reflexes were unable to communicate that. Thus, using an Eye Tracker is very helpful in many experiments because it provides data beyond the participant's behavioral output.

The lab aims to combine studies of the Eye Tracker with studies about Context Memory. For example, I was involved in testing for an experiment where participants were presented with faces (the target) wearing varying types of hats (the context) and an Eye Tracker recorded each saccadic eye movement throughout the learning and testing stages. This is important because it is possible to gauge the minimum number of saccadic movements to the context in order to achieve a Context Effect.

Lastly, the lab specializes in treatments for patients who suffer from Traumatic Brain Injury (TBI).The lab tests various forms of experimental therapies and experiments on the patients in attempt to enhance their Working Memory and to discern whether results in CE experiments vary between healthy and TBI patients. Throughout the summer, I interacted with such patients in Beit Levenshtern, Rana'ana, and The Rehabilitation Center for Veterans after TBI, Yafo.

COGNITIVE NEUROPSYCHOLOGY :: ANAKI LAB

Shonna Schneider (Stern College) "Faces in the Face of Death: Effects of Mortality Salience on Electrophysiological Perception of Facial Expressions"

The focus of our experiment was to systematically examine the influence of facial expressions on neuronal activity in the context of mortality salience, which was measured using ERP (Event-Related Potential). In the framework of the Terror Management Theory, anxiety was associated with an existential threat caused by facial expressions and recognition when presented with mortality salience conditions. However, there are contradictions in the literature about the nature of this relationship, which may be due to the various stages of awareness of death (proximal vs. distal). In this study, participants were proximally presented with mortality salience.

We measured electrophysiological components activated in response to threatening (fear / anger), negative (sadness / disgust), positive (happy) and neutral faces. Participants were given either the pain condition, which entails writing about a painful visit to the dentist, while seeing the word pain flashed between each facial expression, or the death condition, where participants had to write about what they expect their own death to be like, while the word death flashed between each facial expression.

In the results (Tables 1-4) we found significant differences in the P1 and N170 components between the mortality salience condition and the pain condition. In the P1 component, which measures arousal, there is a significant difference between the pain and mortality salience conditions. Participants in the mortality salience condition showed higher arousal to the various facial expressions. Additionally, we discovered a strong incongruence in the N170 (the facial recognition component) between the right and left sides of the brain. For the pain condition, there was a much higher electrophysiological response on the right side of the brain. This finding is congruent with previous research that demonstrates higher arousal in the right side of the brain in the context of facial expressions and emotions. Fascinatingly, in the death salience condition, recognition in the left side of the brain increased tremendously, while it deteriorated in the right side. This experiment suggests that the amplitude of the N170 will be higher in the left side of the brain when presented with facial expressions in the context of mortality salience.

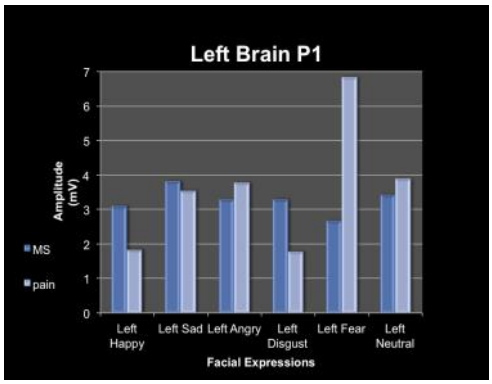

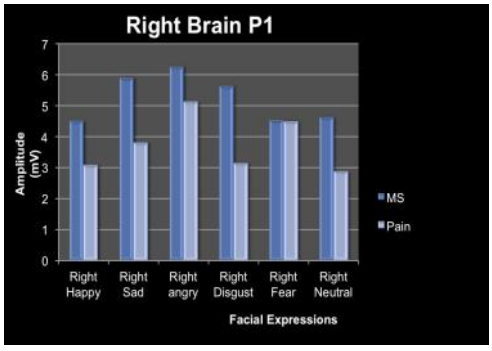

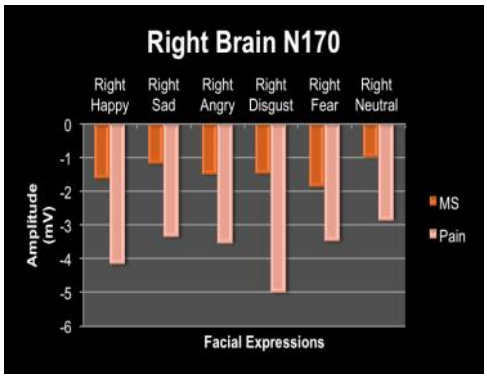

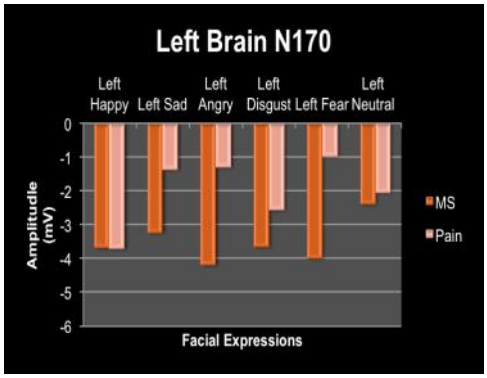

NEUROSCIENCE :: GOLDSTEIN LAB

Deborah Watman (Macaulay Honors College) "Using Magnetoencephalography (MEG) to Understand Connectivity Measures in Individuals with Schizophrenia"

Schizophrenia is a prevalent mental disease that may be recognized by positive and negative symptoms. Patients who display positive symptoms will experience what neurotypicals will not, such as delusions, disordered thoughts, jumbled speech and hallucinations. It is suggested that such symptoms may result from loose brain networks. On the other hand, when there are tight networks, patients may display negative symptoms, including a lack of emotion, memory, and speech.

Magnetoencephalography (MEG) neuroimaging allows us to compare the brain connectivity of patients who have schizophrenia to neurotypicals. With a 248-channel magnetometer array (4-D Neuroimaging, Magnes 3600 WH) in a magnetically shielded room, the MEG records the magnetic field around the head. Because this field is not influenced by biological substances, localizing the origin of the magnetic field in the brain is possible. In addition, the MEG has a very high temporal resolution which makes it ideal for detecting brain activities along the time course of activation.

The MEG recorded the resting state of 42 patients with schizophrenia and 26 neurotypicals as a control group. The subjects kept their eyes open for two minutes and then closed for another two minutes. Before comparing the brain networks of those with schizophrenia who experience mainly positive symptoms to those with mainly negative symptoms, in reference to neurotypicals, the data from each subject must be cleaned from artifacts.

Using MATLAB (Mathworks, Natic, MA) heartbeat artifacts were removed using an event-synchronous cancellation algorithm (Tal and Abeles, 2013). Using Fieldtrip toolbox for MATLAB (Oostenveld, Fries, Maris, and Schoffelen, 2011), data was segmented into two seconds epochs (trials) and epochs displaying power jumps and/or muscle artifacts, a result of the subject making any sort of movement, were visually rejected. The remaining trials were then filtered (1-40Hz) and normalized. We ran Independent Component Analysis (ICA) which allowed us to visualize the components comprising the data in order to find the eye movements, blinks and any additional artifact (see figure 1), and remove such components. Trials were again visualized individually and those displaying artifacts were removed.

After the entire cleaning process, brain networks will be assessed using connectivity measures (e.g., phase lag index and coherence). We assume that in comparison to neurotypical brain networks, individuals with schizophrenia experiencing mainly positive symptoms will have a widespread network, containing more brain areas. However, the connection between the ares will be looser, thereby causing some of the positive symptoms. Individuals with schizophrenia displaying mainly negative symptoms will have MEG scans showing tighter brain networks that are comprised of fewer brain areas. The visualization of such areas made possible by the MEG will allow researchers to further understand the causes and implications of positive and negative symptoms.

This research was under the guidance of Dr. Maor Wolf and Dr. Avi Goldstein.

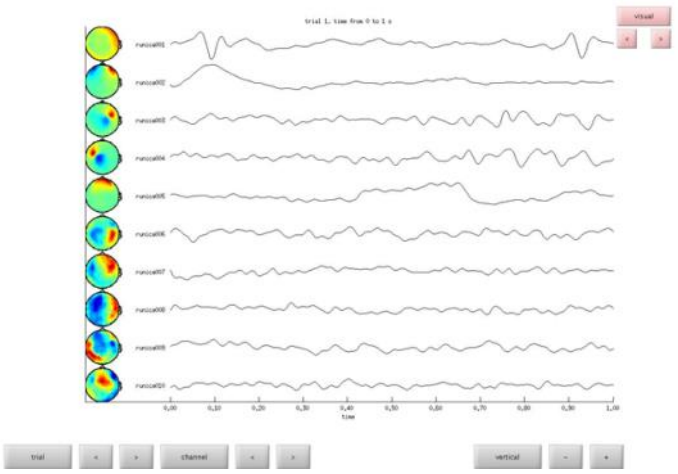

Figure 1. The Results of Independent Component Analysis. The components and data after running ICA on one subject's MEG data. Runica001 contains heart beats artifact. Runica002 contains eye-blinks artifact. Runica005 contains eye movement artifact. Such components would be removed from the data to ensure accurate analysis.

COGNITIVE PSYCHOLOGY :: GLICKSOHN LAB

Batsheva Weisinger (Stern College) "The Effects of Photic and Auditory Stimulation on Time Production as Influenced by the Method of Counting"

There is an established connection between photic stimulation and altered states of consciousness. Previous research in this field has characterized this connection under three particular cardinal frequencies, 6,10, and 18 Hz, corresponding to recorded EEG brainwave frequencies at varying levels of consciousness. Altered time perception and production is a recorded symptom of altered states of consciousness; it has long been understood that a subject cannot tell the passing of time in the same manner when sleeping and when awake. This study is meant to elucidate the role of photic stimulation in the altered time perception that accompanies altered states of consciousness. By having the subject produce time intervals under these three frequencies of photic stimulation, as well as a control condition, a trend should emerge as to the influence of the particular frequency on the perception of time. Additionally, an instructional element was included, indicating to the subject 4 different means by which to demarcate the passing of time. This factor was included to better understand the internal clock itself and as to whether it can be manipulated by the method of counting. An additional factor of auditory stimulation was included when it was noted that the photic stimulator being used also produced a sound with every flash of light. Three conditions, light and sound, just light and just sound were tested with all of each of the frequency x instruction combinations.

NEUROSCIENCE :: SUSSWEIN & WELLER LABS

Lauren Weiss (Stern College) "Nitric Oxide (NO) Donor SNAP Effect on Appetitive Behaviors in a Rat Model"

There Nitric oxide (NO) is a unique second messenger not only because it is a free radical but also because it is a gaseous, inorganic, uncharged diatomic molecule that is so structurally simple that it cannot conceivably be recognized by proteins through the weak intermolecular forces that typify the recognition of other second messengers (Toledo Jr. et al ., 2012). Since NO is an uncharged and almost non polar molecule, it is transported by simple diffusion.

There are three types of nitric oxide synthases (NOS). They are complex proteins found constitutively in two isoforms, neuronal (nNOS) and endothelial (eNOS). The third, inducible, type (iNOS) is rarely present normally but can be expressed in numerous cell types (prototypically in macrophages, mainly in microglia in the CNS) when subjected to immunological challenge.

In mammals, NO is mainly produced from the oxidation of the amino acid L-arginine in a highly controlled process catalyzed by specialized NOS. A number of studies regarding energy intake and neuropeptides has shown that NO is involved in the regulation of food intake in several species such as: mice, rats, chickens and more.

The preliminary experiments on nitrergic regulation of feeding in rats were designed to imitate earlier data on nitrergic control of Aplysia feeding. The effects of the NO donor S-Nitroso-N-acetyl-penicillamine (SNAP) and of the NO precursor L-arginine on Aplysia feeding were previously examined in Professor Abraham J. Susswein's lab. In hungry animals, injecting SNAP had minimal effects on feeding behavior (Katzoff, A. et al.,2002). However, when food was removed from animals after they have been satiated (steady state), it induced a gradual transition to eating large meals when food will be available. Treatment with the NO donor was one of several stimuli that preserved the steady-state, thereby inhibiting feeding (Miller, N. et al.,2012). This experiment suggests that post-ingestion NO formation derived from food eaten during snacks could be a post-ingestion stimulus that preserves the steady-state inhibition of feeding. Susswein's lab speculated that increased L-arginine and extracellular NO are weak inhibitors of feeding.

These studies indicate that L-arginine and NO are weak inhibitors of feeding and are most effective in conditions of relatively low drive to eat, such as when animals are in the steady-state, and

eat snacks rather than large meals. We therefore devised an experimental situation in which rats have a relatively low drive to eat, but some eating occurs.

Moreover, pervious studies in mammals reported that NO is related to obesity, insulin resistance and more. However, not any of these studies focused on the influence of background NO release, after satiation.

Our aim is to examine the hypothesis that NO, and its precursor L-arginine, have a role in regulating feeding, and could therefore have a role in either the reason of feeding disorders, or in their treatment. The hypothesis is based on the idea that metabolites can act as post-ingestive or homeostatic signals that affect subsequent feeding behavior. In some cases metabolites are precursors of neurotransmitters, and affect feeding and other behaviors by regulating transmitter synthesis and release. We propose that the NO donor SNAP will inhibit feeding via an increase in NO.

The experiment was performed in the morning hours between 9:30am-12:00 pm on young adult male Wistar rats, 70-90-days-old, (mean weight: 250-300 g, respectively). We gave the rats 60% of their regular consumption of chow night before the experiment. In the morning of the experiment the rats were given 20 g. of chow for half an hour. The injection of SNAP was given intraperitoneally (i.p), and given to all subjects in a counterbalanced design of different dosages of: 0 (saline), and 10 mg/kg. Next, the rats were given 20 g. of chow, we monitored food consumption for one hour and at the end of the hour we weighed the food to check the influence of SNAP on food consumption.

Treatment with SNAP led to a decrease in grams of chow eaten (see figure A) and a decrease in the number of meals eaten within one hour (see figure B) compared to the control group which was treated with saline (*p<0.05).

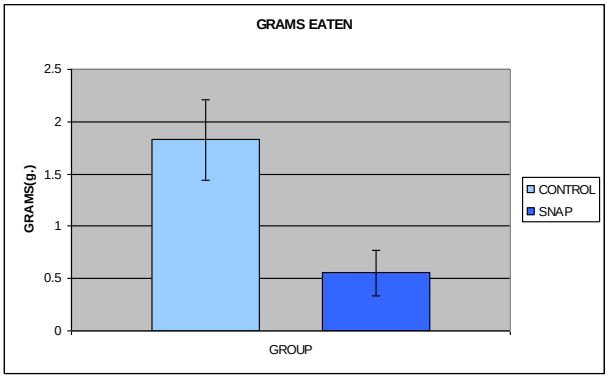

Figure A .

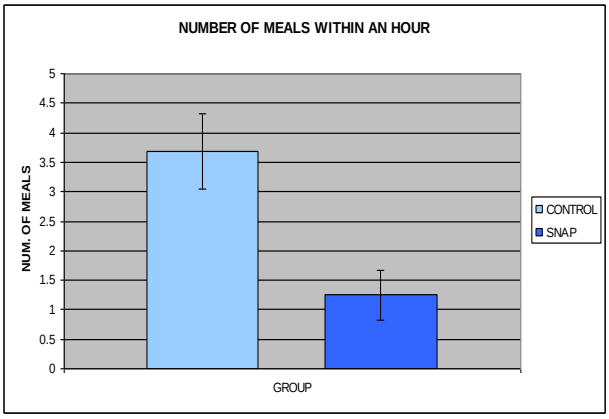

Figure B .